Journal of Non-Crystalline Solids 473 (2017) 1–16

Contents lists available at ScienceDirect

Journal of Non-Crystalline Solids

journal homepage: www.elsevier.com/locate/jnoncrysol

Impacts of composition and beta irradiation on phase separation in multiphase amorphous calcium borosilicates

Karishma B. Patel[a,*], Bruno Boizot[b], Sébastien P. Facq[a], Sylvain Peuget[c], Sophie Schuller[d], Ian Farnan[a]

[a] Department of Earth Sciences, University of Cambridge, Downing Street, Cambridge CB23EQ, UK
[b] Laboratoire des Solides Irradiés, CNRS-UMR 7642, CEA-DRF-IRAMIS, Ecole Polytechnique, Université Paris-Saclay, Palaiseau Cedex, 91120, France
[c] CEA, DEN, DE2D, SEVT, LMPA, Marcoule, F-30207 Bagnols-sur-Cèze, France
[d] CEA, DEN, DE2D, SEVT, LDPV, Marcoule, F-30207 Bagnols-sur-Cèze, France

ARTICLE INFO

Keywords:
Nuclear waste materials
Calcium borosilicate glasses
Phase separation
Radiation effects
Microstructure
Crystallization

ABSTRACT

Borosilicate glasses for nuclear waste applications are limited in waste loading by the precipitation of water-soluble molybdates. In order to increase storage efficiency, new compositions are sought out that trap molybdenum in a water-durable $CaMoO_4$ crystalline phase. Factors affecting $CaMoO_4$ combination and glass-in-glass phase separation in calcium borosilicate systems as a function of changing [MoO_3] and [B_2O_3] are examined in this study in order to understand how competition for charge balancers affects phase separation. It further examines the influence of radiation damage on structural modifications using 0.77 to 1.34 GGy of 2.5 MeV electron radiation that replicates inelastic collisions predicted to occur over long-term storage. The resulting microstructure of separated phases and the defect structure were analyzed using electron microscopy, XRD, Raman and EPR spectroscopy prior to and post irradiation. Synthesized calcium borosilicates are observed to form an unusual heterogeneous microstructure composed of three embedded amorphous phases with a solubility limit ~2.5 mol% MoO_3. Increasing [B_2O_3] increased the areas of immiscibility and order of $(MoO_4)^{2-}$ anions, while increasing [MoO_3] increased both the phase separation and crystallization temperature resulting in phases closer to metastable equilibrium, and initiated clustered crystallization for [MoO_3] > 2.5 mol%. β-irradiation was found to have favorable properties in amorphous systems by creating structural disorder and defect assisted ion migration that thus prevented crystallization. It also increased reticulation in the borosilicate network through 6-membered boroxyl ring and Si ring cleavage to form smaller rings and isolated units. This occurred alongside an increased reduction of Mo^{6+} with dose that can be correlated to molybdenum solubility. In compositions with existing $CaMoO_4$ crystallites, radiation caused a scattering effect, though the crystal content remained unchanged. Therefore β-irradiation can preferentially prevent crystallization in calcium borosilicates for [MoO_3] < 2.5 mol%, but has a smaller impact on systems with existing $CaMoO_4$ crystallites.

1. Introduction

High-level nuclear waste (HLW) has been successfully incorporated into borosilicate glasses and vitrification proves a reliable and established technique [1]. Amorphous structures are ideal waste form candidates as they are able to incorporate a wide array of nuclides with varying charge and are resistant to internal radiation [2]. Moreover, they can be synthesized at reasonable conditions and show good chemical stability when subjected to aqueous environments [1,3]. Though they have proved beneficial in many regards, there are material limitations introduced by insoluble species that can result in unexpected phase separation [4–6] and thus degradation of physical properties [7,8].

The waste loading in French nuclear waste glass R7T7 is limited to 18.5 wt% fission products [9], which corresponds to ~1 mol% MoO_3 [10]. Above this solubility limit, it is possible for metastable phases to form leading to crystallization of molybdenum-rich phases [11,12]. The production of alkali molybdates (Na_2MoO_4, Cs_2MoO_4), known as yellow phase, are particularly problematic owing to their high water solubility and ability to act as carriers for radioactive cesium and strontium [1,13]. This ability thus creates a contamination risk during final geological deposition by increasing corrosion probabilities [14,15]. While formation of yellow phase can prove detrimental to chemical durability, alkaline earth molybdates ($CaMoO_4$) are

* Corresponding author.
E-mail address: kp391@cam.ac.uk (K.B. Patel).

http://dx.doi.org/10.1016/j.jnoncrysol.2017.06.018
Received 25 April 2017; Received in revised form 14 June 2017; Accepted 15 June 2017
Available online 02 August 2017

comparatively water durable and are stable following synthesis in a borosilicate matrix [12,14,15].

Selective and controlled formation of secondary phases can be useful to accommodate waste streams with a high concentration of insoluble elements while maintaining physiochemical properties. This notion has led to a renewed interest in glass ceramic (GC) materials. GCs contain a combination of vitreous and crystalline phases that can be compositionally induced during glass synthesis, or through a separate heat treatment. They can also be specifically manufactured by dispersing solid particles in a liquid [1]. These structures are ideal candidates for legacy waste containing refractory oxides or for post operation clear out, where waste has high molybdenum or alkali concentrations that would otherwise require unacceptably high melting temperatures. They are also useful to trap volatile elements such as Cs in a crystalline framework, which would otherwise prove problematic in conventional high temperature vitrification techniques.

Molybdate formation in particular can be controlled by composition [10,16,17], external heat treatments [12,18,19], redox chemistry [20,21], or by controlled cooling during synthesis [11]. Compositionally, the preferential charge balancing of $(BO_4)^-$ and $(MoO_4)^{2-}$ anionic entities by Na^+ and Ca^{2+} cations can determine molybdate speciation and network connectivity [22]. Due to charge, mobility, size and sterics $(BO_4)^-$ prefers Na^+ ions as charge balancers. This preference thus enables the incorporation of Ca^{2+} ions into molybdates [4,23,24]. It is observed that an increase of B_2O_3 will reduce the tendency of Na_2MoO_4 crystallization and increase the crystallization of $CaMoO_4$ in soda-lime borosilicates [10,24]. A similar effect has also been observed when the concentration of CaO is increased, owing to a corresponding reduction of $(BO_4)^-$ species [10,22]. Increasing the quench rate to 10^4 °C.min^{-1} has also been observed to promote the growth of $CaMoO_4$ over alkali molybdates and increase molybdenum solubility up to 2.5 mol% MoO_3 [12].

While composition and quench rate can directly influence molybdate speciation, redox chemistry is known to affect molybdenum solubility. Molybdenum can exist in several oxidative states (Mo^{6+}, Mo^{5+}, Mo^{4+}, Mo^{3+}), but in oxidizing or neutral conditions molybdenum ions will be primarily hexavalent [21]. The high field strength of Mo^{6+} exerts a strong ordering effect on the surrounding oxygen atoms and results in tetrahedral $(MoO_4)^{2-}$ units [15,16,24]. These tetrahedra remain unconnected to both the glassy framework and to each other, and are found embedded in a cationic lattice located in non-bridging oxygen (NBO) channels according to Greaves' structural model [25]. In this configuration, cations are octahedrally coordinated and bound to $(MoO_4)^{2-}$ entities by weak long-range ionic forces [17]. A reducing environment on the other hand, is found to promote molybdenum species in lower oxidative states that subsequently increases the solubility of molybdenum groups in borosilicates and silicates [15,21].

Though these relationships have been investigated in soda-lime borosilicates, very little research describes the simplified calcium borosilicate system. It is imperative to understand this system if we are to drive the selective formation of $CaMoO_4$ at high concentrations of MoO_3 in nuclear waste materials. This study seeks to address the effect of preferential charge balancing of $(BO_4)^-$ and $(MoO_4)^{2-}$ units in the absence of Na^+ alkali ions to determine the specific effect of $[B_2O_3]$ on the precipitation of $CaMoO_4$ and subsequent response of the residual matrix. This investigation further seeks to investigate how ionizing irradiation will alter both the crystalline and amorphous microstructures in terms of promoting or remediating phase separation.

Internal radiation from nuclear waste will constitute localized high-energy input events that can significantly alter the structure of a material. For the first 100 to 300 years of high-level waste storage, β-decay will provide a higher ionization dose than α-decay [26], thus resulting in significant alteration to the encapsulating structure. The dose from β-decay will then reach a plateau from 100 to 10^6 years of storage given current waste loading for French nuclear waste glasses. In organized systems such as metals or crystals, accelerated external radiation used to replicate these events can induce dislocations and eventual cracking along stress planes, as well as swelling and void formation [7,26]. These phenomena also take place in glasses irradiated by electrons where they are initiated by the formation of point defects [27,28]. These composition dependent defects can further lead to the release of charge compensators that can enable alkali migration and formation of alkali clusters [28], as well as the creation of molecular oxygen [29] following either β or x-ray irradiation [30,31]. Alkali migration and clustering can foster the creation of a precursor environment for molybdate formation; hence, it is a factor governing precipitation during long-term storage. Accumulated defects can also lead to glass-in-glass phase separation [26,32]. Alteration to the internal structure and connectivity of amorphous phases is of significance, as modification can result in changes to macroscopic properties such as density and hardness [33,34].

Molybdate formation and radiation effects on homogeneous borosilicates have been independently examined, but very few studies correlate the effects of radiation on phase separation and even fewer investigate the calcium borosilicate system. In this study, we segregate the effects of changing $[B_2O_3]$ and $[MoO_3]$ independently on the microstructure and solubility of molybdenum entities on a fundamental level to better understand the tendencies of internal phase separation. This study further attempts to determine if internal radiation produced from radioisotope β-decay on the order of 100 to 10^6 years of storage will induce, propagate or anneal glass-in-glass or crystalline phase separation in these samples, thus providing a window to long-term structural projections in these systems.

2. Experimental

2.1. Glass compositions and synthesis technique

In this study we synthesized several non-active glasses and glass GCs to test the solubility of molybdenum in calcium borosilicates and the durability of precipitated crystalline phases as a function of $[B_2O_3]$ and $[MoO_3]$ when subjected to β-irradiation. Table 1 provides the normalized glass compositions prepared.

The CB series tests the effect of increasing $[B_2O_3]$, while the $[SiO_2]$/[CaO] ratio remained constant and with a fixed amount of MoO_3 and Gd_2O_3. This series will be used to determine how the concentration of boron will affect the Ca^{2+} ion distribution and preferential charge balancing when the molybdenum content is around its solubility limit and no alkalis are present. Gadolinium was included as a spectroscopic probe for EPR measurements, but rare earths can also be considered as actinide surrogates, indicating incorporation sites of actinide species. The composition of CBO was determined based on the eutectic point of the SiO_2 – CaO system [35] and was used as a marker for boron incorporation sites.

The CM series tests the effect of increasing $[MoO_3]$ in a calcium borosilicate matrix normalized to inactive French nuclear waste glass

Table 1
Sample composition in mol%.

Series	Sample ID	SiO_2	B_2O_3	Na_2O	CaO	MoO_3	Gd_2O_3
CB	CBO	59.41	–	–	38.94	2.50	0.15
	CB7	78.07	7.00	–	12.28	2.50	0.15
	CB15	71.16	15.00	–	11.19	2.50	0.15
	CB23	64.16	23.00	–	10.09	2.50	0.15
CM	CaBSi	67.74	20.97	–	11.29	–	–
	CM1	67.07	20.76	–	11.18	1.00	–
	CM2.5	66.05	20.44	–	11.01	2.50	–
	CM7	63.00	19.50	–	10.50	7.00	–
M	CM5	65.00	22.00	–	8.00	5.00	–
	CM7	63.00	19.50	–	10.50	7.00	–
	CN10	49.90	13.29	10.78	16.03	10.00	–

SON68. It will be able to probe how molybdenum solubility is affected by irradiation when $(BO_4)^-$ and $(MoO_4)^{2-}$ entities must compete for charge compensators. The third sample set, the M series, tests the effects of matrix variation on $CaMoO_4$ crystallite formation while the [CaO]/[MoO_3] ratio is kept constant. Note that CM7 is in two of the series and CN10 introduces Na into the system for coherency with literature.

Glass batches of ~30 g were prepared by mixing and then melting powders of SiO_2, H_3BO_3, $CaCO_3$, Na_2CO_3, MoO_3 and Gd_2O_3. Synthesis was conducted at atmosphere in a platinum-rhodium (90/10) crucible. All glasses were melted at 1500 °C for 3 h, with the exception of CN10 that had only a 30 min time at temperature to prevent the volatilization of Na. The glasses were then crushed and remelted at 1500 °C for 2 h. Only CBO and CN10 could be cast at room temperature on a graphite-coated iron plate. The remaining samples were too viscous to be poured and were quenched using a water bath and tapped out of the crucible with a hammer. All glasses and glass fragments were annealed for 24 h at 520 °C to reduce internal stresses.

Samples were roughly cut to a thickness of 1 mm and were ~3 mm^2 in surface dimensions to fit the irradiation sample holder. They were then hand polished successively using P600, 800, 1200, 2400 and 4000 SiC grit paper to achieve a uniform thickness of approximately 500 μm. This ensured homogeneous β-irradiation throughout the material. Samples were subsequently diamond polished using a dimple grinder with 3 μm and 1 μm diamond paste.

2.2. Irradiation experiment

Electron irradiation is a tool used to replicate the damage observed following inelastic collisions caused by internal β-decay within a nuclear waste material on an accelerated timeline [26]. The β-irradiation emulated in this experiment was performed with 2.5 MeV electrons from the Pelletron accelerator (SIRIUS facility) at LSI in Palaiseau, France. In order to keep the maximum temperature of the sample holder at 50 °C and mitigate temperature induced structural recovery, an average current of 15.8 μA was used. With these beam specifications, doses of 0.77 GGy and 1.34 GGy were achieved on two separate sample sets. A GGy is on an order of magnitude consistent with 100 to 10^6 years of storage for 18.5 wt% actinide waste loading [8,26], thus replicating expected long-term damage.

2.3. Sample characterization

Morphology, composition and crystal phase determination were investigated using X-ray diffraction (XRD) and Scanning Electron Microscopy (SEM). Combined, these techniques were able to determine amorphous-amorphous phase transformations versus phase separation and precipitation of crystalline phases. In this context, phase transformations refer to changes in material properties resulting from alterations in the connectivity of amorphous network formers for a fixed composition.

XRD was performed with $CuK\alpha_1$ (λ = 0.15406 nm) and $CuK\alpha_2$ (λ = 0.15444 nm) wavelength on a Bruker D8 ADVANCE equipped with Göbel mirrors for a parallel primary beam and a Vautec position sensitive detector. Spectra were collected for a 2θ = 10–90° range with a 0.02 step size and 10 s per step dwell time. Samples were left as monoliths to isolate irradiation effects and to avoid additional structural changes induced by mechanical force required to powder samples. Structural analysis and crystallite size valuations were performed using whole pattern Rietveld refinements with the software Topas v4.1 [36]. Single parameter crystal size (CS) estimates were made using the Scherrer equation, which is a function of peak shape and width. Strain was not included in fitting as the correlation between size and strain is too high due to the large amorphous content, which has been discussed elsewhere [37].

SEM backscattered (BS) imaging was performed on a Quanta-650F at low vacuum (0.06–0.08 mbar) with a 5 keV beam resulting in a penetration depth of ~1 μm. Images were collected using FEI Maps software. EDS was likewise performed at low vacuum, but with a 7.5–20 keV beam using an 8 mm cone in order to reduce skirting effects. This configuration gave insight on the interface between phases and the relative composition of each phase to be identified. In certain cases, electron backscatter diffraction (EBSD) equipped with a Bruker e^-Flash^{HD} detector was additionally utilized at low vacuum and with a 20 keV beam and current of ~10 nA to detect trace crystallites. A 70° tilt and an alumina reference were employed for optimal detection and phase recognition. Acquisition and analysis for both EBSD and EDS were made using Bruker ESPRIT software.

Raman Spectroscopy was utilized to determine relative structural changes induced by composition and irradiation in all phases. It is particularly useful in analyzing the local environment of non-diffracting amorphous phases, as well as small volumes of crystallites. Raman spectra were collected with a 300 μm confocal hole over the 150–1600 cm^{-1} spectral range using a confocal Horiba Jobin Yvon LabRam300 spectrometer equipped with a holographic grating of 1800 grooves per mm and coupled to a Peltier cooled front illuminated CCD detector (1024 × 256 pixels in size), resulting in a spectral resolution of ~1.4 cm^{-1} per pixel. The excitation line at 532 nm was produced by a diode-pumped solid-state laser (Laser Quantum) with an incident power of 100 mW focused on the sample with an Olympus 50 × objective.

Many β-irradiation induced structural changes observed using the aforementioned analysis techniques are a repercussion of changes to the electronic structure. Electron Paramagnetic Resonance Spectroscopy (EPR) is a unique method employed to directly probe the structure of unpaired electrons in the bulk material, which may be responsible for longer-range modifications. EPR spectra were obtained at the X-band (ν ~ 9.86GHz) on an EMX Bruker spectrometer at room temperature with 100 kHz field modulation and 1 mW microwave power using quartz tubes. EPR spectra were normalized to the relative sample weight, attenuation and receiver gain. All recorded defects were induced by irradiation.

3. Results

3.1. Microstructure and crystallinity

3.1.1. Immiscibility

The microstructure of all pristine samples was investigated using SEM imaging. Using this technique 2–3 phases were detected in the CB series and some of the samples in the CM series (see Fig. 1). This unusual microstructure showed embedded immiscibility, a schematic of which can be seen in Fig. 2. EDS analysis indicates that there are CaMo-rich droplets (phase B) are embedded within a *Si*-rich matrix (phase A). Within these CaMo-rich droplets (phase B), there are further immiscible regions 5–50 μm in diameter (phase C) that are also rich in Si. Fig. 3 provides quantitative micrographs to support these. Furthermore, the presence of phase C was observed to be dependent on the initial size of phase B regions. In some cases no phase C deposits were observed when the area of phase B was very small. This observation suggests that phases A and B separate from the melt concurrently during synthesis and that phase C forms following a mixing of phase A with the surrounding phase B during cooling.

According to EDS analysis, phase A and C are rich in Si and phase B is poor in Si. While this is true, phase C is compositionally a mixture of phase A and B and is dependent on the droplet area and therefore probed volume. In the CM series, phase C has a [Si]/[Ca] ratio of ~9.0–9.3 relative to phase A with [Si]/[Ca] ~ 40–58 as determined by EDS analysis, which assumed each element was found as an oxide. Similarly, the [Si]/[Ca] ratio for phase C is ~13–44 relative to [Si]/[Ca] ~ 32–62 for phase A in the CB series. A greater range for [Si]/[Ca] was observed in the CB series, indicating that the B_2O_3 content

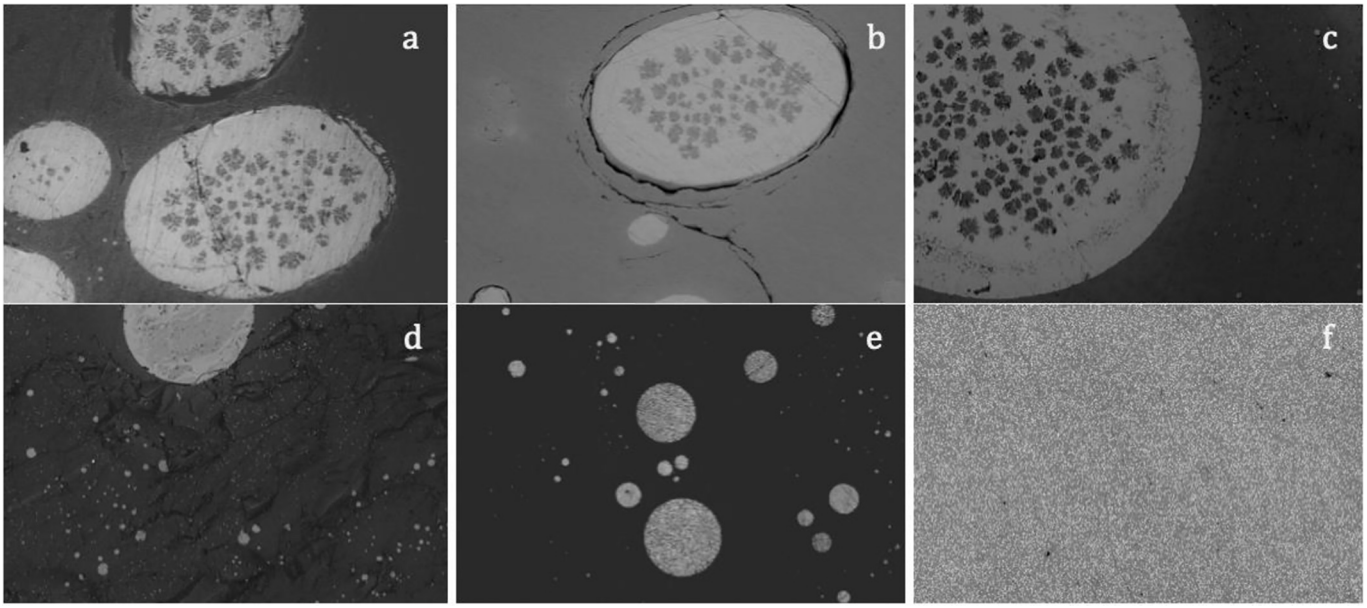

Fig. 1. Microstructure of select samples prior to irradiation: a) CaBSi; b) CM1; c) CM2.5; d) CM7; e) CM5 and f) CN10. Micrograph dimensions: 200 μm × 300 μm. Lighter phase is CaMo-rich and darker phase is *Si*-rich. Samples CM7, CM5 and CN10 further exhibit $CaMoO_4$ crystallization.

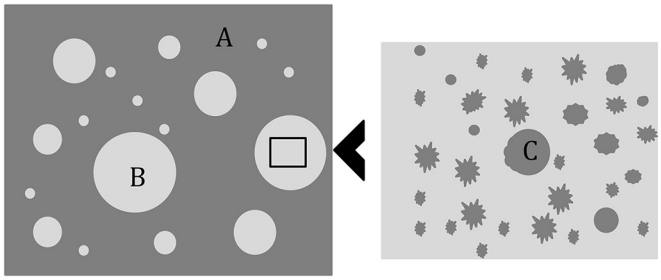

Fig. 2. Schematic of observed embedded immiscibility in the microstructure of CB7, CB15, CB23, CaBSi, CM1 and CM2.5. Phase A, B and C are used in text, where A and C are *Si*-rich and B is Ca-rich and is the preferential carrier of Mo groups. Quantitatively C appears to be a mix of A and B, with a bias towards phase A.

significantly impacts the distribution of both Si and Ca atoms between phases in heterogeneous systems in comparison to MoO_3 additions.

3.1.2. Concentration effects on pristine samples

The microstructure observed in Fig. 1 reflects the immiscibility of CaO within a *Si*-rich phase given the current synthesis conditions, which is accentuated by the addition of MoO_3. As the difference in [CaO] between samples is not very significant, microstructural variations between the multi-amorphous phases in terms or size, morphology and distribution of phases B and C can be directly correlated to increasing $[B_2O_3]$ and $[MoO_3]$.

In the CB series, the effect of increasing $[B_2O_3]$ causes changes to the morphology and density of the various amorphous phases. In CB7, phase B deposits are bimodal in size distribution with mainly two size categories: small (2–18 μm) and medium (75–150 μm). As $[B_2O_3]$ increases, the number of phase B deposits increases and larger deposits (> 200 μm) are also observed, indicating an increase in the population density of phase B. Furthermore, there are changes to the distribution of phase C droplets within phase B separative regions. In general, phase C deposits were only found in medium and large separative regions of phase B and were ~3–18 μm in diameter. In some larger regions of phase B, clusters of phase C deposits around ~50 μm in diameter were also observed. Therefore CB7 had few phase C deposits, but with increasing $[B_2O_3]$ the number of deposits increased though the individual size of deposits did not vary significantly. A change in the physical distribution of phase C deposits within phase B was also observed. With increasing $[B_2O_3]$, the deposits of phase C along the interface of phase A and B became larger, as compared to those found in the center of separated phase B (see Fig. 4b–c).

Quantitatively, the [Ca]\[Mo] ratio increases as we move away from the A-B interface and into phase B and it decreases as we move into phase A in the CB series. This is a result of Mo clustering on the phase B-side of the interface and a Ca-rich region along the phase A-side of the interface. As $[B_2O_3]$ increases, a drop in the relative amount of Si in phase B and C is observed, alluding to phase B being rich in boron.

Similar to the CB series, the glasses CaBSi, CM1 and CM2.5 in the CM series also exhibit three phases with embedded immiscibility

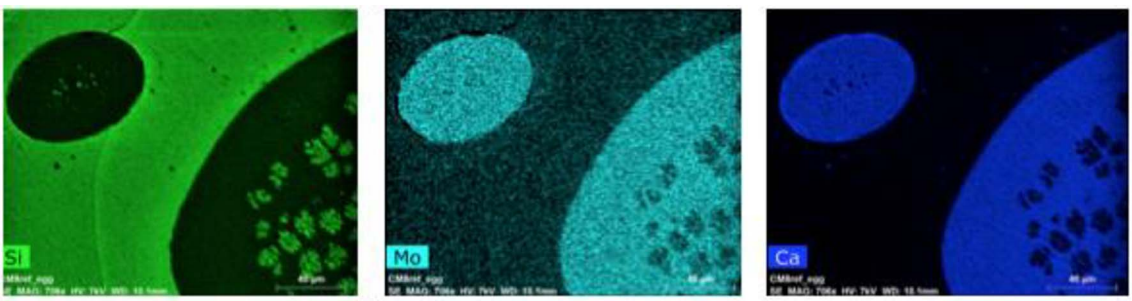

Fig. 3. SEM EDS maps of CM1 exhibits three phases, where one (phase C) is a mix of the other two and is embedded in the CaMo-rich droplets (phase B).

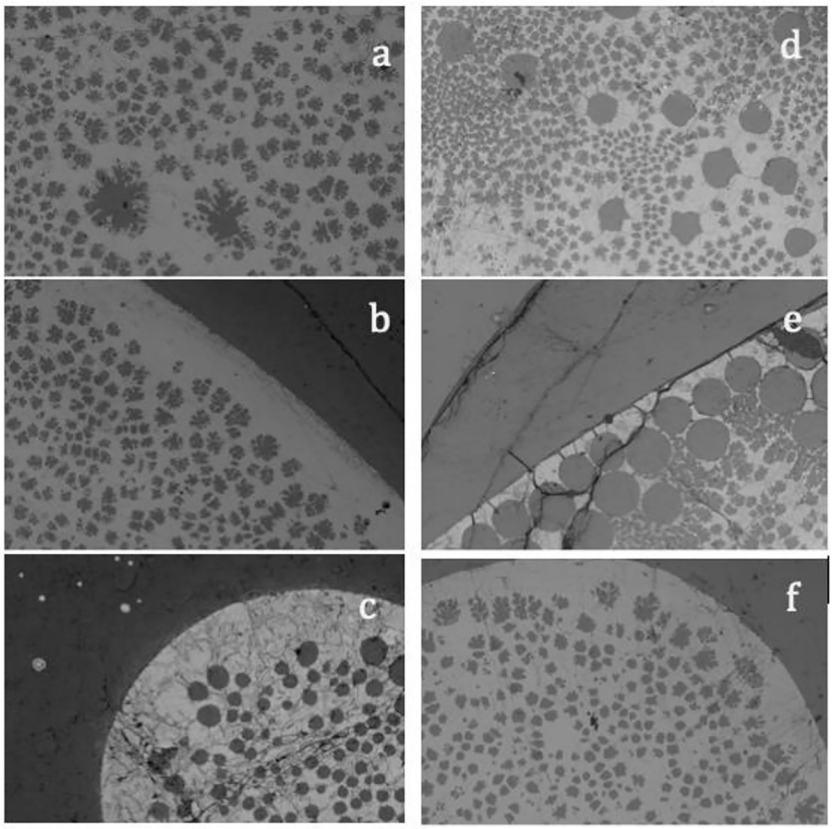

Fig. 4. SEM micrographs of CB15 prior to irradiation (a, b) and following 1.34 GGy of β- irradiation (d, e), and of CB23 prior to irradiation (c) and following 1.34 GGy of β-irradiation (f). Images are from two distinct samples that represent pristine and irradiated conditions.

(Figs. 1 and 3). As [MoO_3] increases from 0 to 2.5 mol%, phase B region of immiscibility become more spherical in morphology and increase marginally in size. Unlike the CB series, larger phase C deposits are found in the center of separated phase B and the smaller phase C deposits are located near the interface between CaMo-rich regions and the outer *Si*-rich matrix (B-A interface). This latter result indicates how increasing [MoO_3] causes direct changes to the melt viscosity and therefore to the distribution and size of phase C deposits within phase B separative regions. Quantitatively, we observe an increase of [Mo] and a decrease of [Si] in phase B as [MoO_3] increases. Conversely, an increase of [Si] is observed in phase A.

Despite a heterogeneous microstructure and varying compositions, all of the samples mentioned above with embedded immiscibility (CaBSi, CM1, CM2.5, CB7, CB15 and CB23) are fully amorphous according to XRD.

As the concentration of MoO_3 exceeds 2.5 mol% in CM5, CM7 and CN10, GCs are formed in which only two phases are present. Phase A remains amorphous in these GCs and subsequently observes an increase in the amount of Si in the bulk matrix. XRD analysis indicates that the other phase is crystalline with a tetragonal scheelite-type powellite ($CaMoO_4$) structure and an $I4_1$/space-group, see Fig. 5. In this powellite structure, $(MoO_4)^{2-}$ tetrahedra are charge balanced by eight-fold coordinated calcium. The tetragonal cell parameters of powellite determined by full diffractogram Rietveld refinements range between a = 5.226–5.228 Å and c = 11.455–11.462 Å (see Table 2). XRD analysis also displays a wide-angle x-ray scattering signal at ~22° in the diffractogram, representative of the amorphous phase. In these specimens there is no phase C, as is observed in heterogeneous multi-amorphous phase samples.

In calcium borosilicate GCs, $CaMoO_4$ crystallites with a Scherrer crystallite size (CS) ranging between 20 and 125 nm aggregate into larger clusters of varying sizes from 300 nm – 90 μm. These crystal clusters are randomly distributed in an amorphous matrix, see Fig. 6.

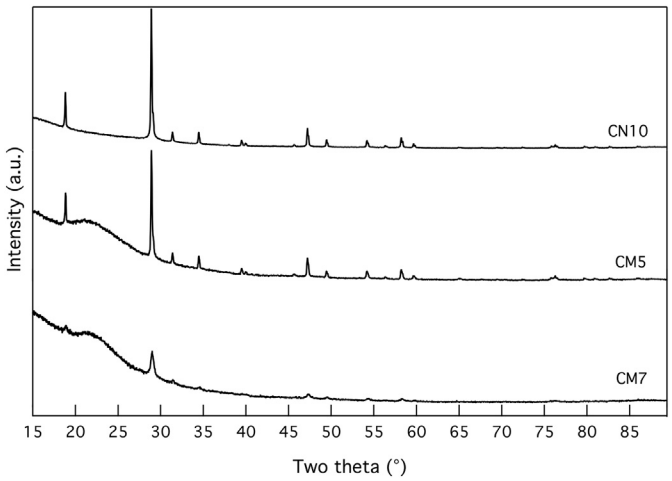

Fig. 5. XRD patterns of $CaMoO_4$ bearing samples in the M series.

While the distribution in aggregate size does not vary significantly between the two calcium borosilicate GCs, Table 2 indicates that the CS are smaller in CM7 despite a higher [MoO_3] than CM5. This result indicates that the composition of the residual matrix has a significant influence on CS, possibly more so than [MoO_3] when [MoO_3] > 2.5 mol%. In CM5 the SiO_2/B_2O_3 ratio is ~2.95, while in CM7 the SiO_2/B_2O_3 ratio is ~3.30. This relative difference suggests the influence of increasing [B_2O_3] on increasing the general order of $(MoO_4)^{2-}$ units and hence promoting CS growth.

In comparison to calcium borosilicates, crystallites are found in ~1 μm particles and are uniformly distributed in the soda-lime borosilicate CN10, see Fig. 1(f). This result outlines the importance of alkalis in promoting homogenous crystallite distribution. Furthermore, though the SiO_2/B_2O_3 ratio is ~3.75 in CN10 and the [MoO_3] is double

Table 2
Scherrer crystallite size (CS) diameter and cell parameters from Rietveld refinement of XRD spectra using Topas v4.1 [36].

Sample ID	CS (nm) pristine	*a* (Å)	*c* (Å)	CS (nm) 0.77 GGy	*a* (Å)	*c* (Å)	CS (nm) 1.34 GGy	*a* (Å)	*c* (Å)
CM5	124.92 (± 3.39)	5.2281 (± 0.0002)	11.4618 (± 0.0004)	125.82 (± 6.82)	5.2270 (± 0.0004)	11.4497 (± 0.0013)	153.54 (± 8.69)	5.2270 (± 0.0003)	11.4527 (± 0.0010)
CM7	20.47 (± 0.70)	5.2261 (± 0.0018)	11.4554 (± 0.0051)	21.80 (± 0.78)	5.2169 (± 0.0017)	11.4429 (± 0.0051)	28.23 (± 1.54)	5.2136 (± 0.0018)	11.4126 (± 0.0060)
CN10	125.24 (± 1.94)	5.2264 (± 0.0001)	11.4554 (± 0.003)	130.97 (± 4.13)	5.2256 (± 0.0002)	11.4478 (± 0.0007)	118.53 (± 3.00)	5.2257 (± 0.0002)	11.4402 (± 0.0006)

that of CM5, the CS values are very similar. This observation further alludes to the effect of alkalis on mitigating structural alterations induced by B_2O_3 on $CaMoO_4$ formation during synthesis.

Quantitatively, we observe a similar trend across the amorphous matrix - crystalline interface as we do across the phase A - B interface in multi-amorphous phase samples with respect to the [Ca]\[Mo] ratio (see Fig. 7). The gradual changes in [Ca] that are observed to increase as we move towards the center of crystal clusters suggests a diffusion-based mechanism of formation. While the relatively high [Mo] at the interface suggests an inherent immiscibility between $(MoO_4)^{2-}$ anions and silica.

3.1.3. Radiation effects

The heterogeneous nature of the samples resulted in a variance of features prior to and following irradiation. As such, comparative observations were made on phase B deposits of similar sizes in the three sample sets (1 unirradiated, 2 irradiated). This was based on the observation that microstructural changes following irradiation had different trends for large and small CaMo-rich (phase B) deposits.

In the CB series, changes to the microstructure following irradiation could not be definitely correlated to changing $[B_2O_3]$. In CB7 and CB15 the phase C deposits appeared to coalesce with increasing dose. This effect is predominantly notable along the A-B interface (see Fig. 4d, e).

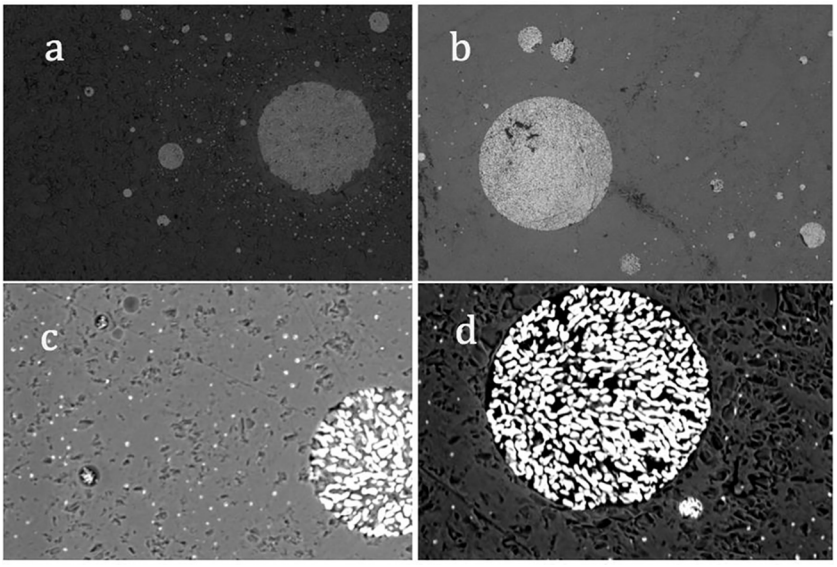

Fig. 6. Microstructure of CM5 prior to irradiation (a, c) and following dose of 1.34 GGy of beta irradiation (b, d). Micrograph dimensions for a, b: 200 μm × 300 μm; and for c, d: 20 μm × 30 μm.

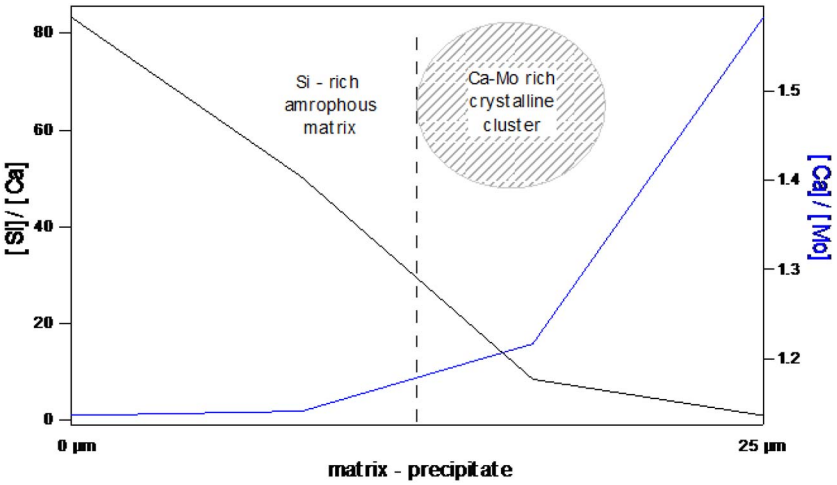

Fig. 7. EDS quantitative analysis of CM5 along the crystalline to amorphous matrix interface.

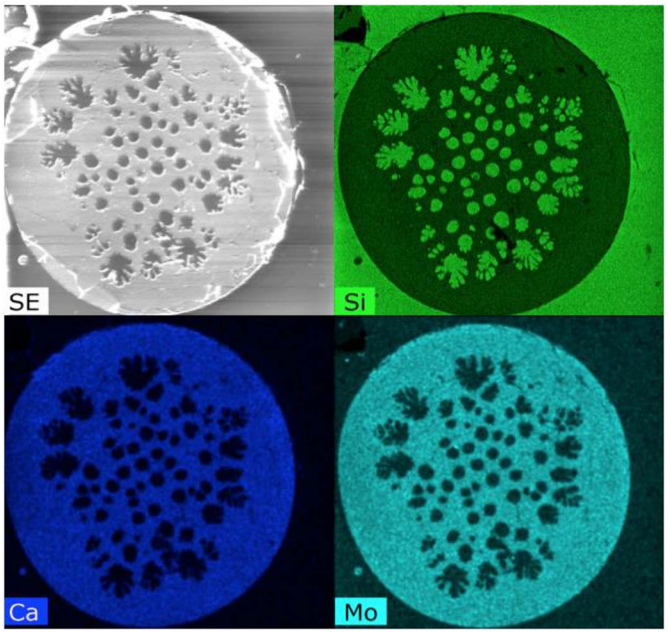

Fig. 8. SEM EDS maps of CB23 irradiated to 1.34 GGy. Micrograph dimensions: 220 μm × 220 μm. In clockwise direction from top right corner: SE image, Si, Mo and Ca.

This change in microstructure indicates reorganization in the CaMo-rich phase B that enables migration and coalescence of phase C droplets, thus enabling Si units to congregate in a phobic - philic type mechanism. Unlike CB7 and CB15, the droplets of phase C along the A-B interface of CB23 are less circular following irradiation (see Figs. 4 and 8). There appears to be a spattering of phase C regions of immiscibility from an originally circular geometry, which is presumed to be a result of increased mixing.

The distribution of phase C deposits in the CB series also appeared to change following irradiation. In smaller deposits of phase B, embedded phase C droplets are larger in the center of phase B regions. Whereas for larger regions of phase B, the droplets are smaller in the center no matter their shape, prior to irradiation. Following irradiation this is still true, as Fig. 8 depicts, but phase C deposits are generally found to be closer to the A-B interface and are larger in this area following irradiation.

The changes to the morphology and distribution of phase C following irradiation collectively imply that the degree of mixing initiated by ionization events was affected by increasing $[B_2O_3]$. Furthermore, a barrier exists for 15 mol% < $[B_2O_3]$ < 23 mol% where immiscible droplets stop coalescing and start mixing following irradiation. Compositionally we still see 3 phases in the CB series 9 see Fig. 8), but there is variation along the interface between phases. EDS analysis across the A-B interface of CB23 in Fig.9 indicates that phase B becomes richer in both Mo and Ca following radiation, though the migration of each element occurs at a different rate. This result reflects phase specific properties that promote or retard cationic movement. It is speculated that Ca migrates on average from phase A to B and C via changes to units being charge balanced. Additionally, Mo migrates to phase B from both phase A and C, hence why a drop in [Ca]/[Mo] occurs in both phase A and B following irradiation (Fig. 9). The trends across the A-B interface following irradiation vary for each composition, but in each case some migration of Ca and Mo is noted either across the phases or towards the bulk from the surface.

While most of the phases in the CB series continued to be amorphous, an exception lies in CB7. Following a dose of 0.77 GGy, CB7 exhibited dendritic crystals as determined by EBSD (see Appendix). As these are only detected by electron microscopy and not XRD, it indicates that the crystal content is below 1 vol%. It cannot be definitively concluded if this crystallization is radiation induced precipitation or caused by formation during synthesis and sampling variations, as the number of samples irradiated is limited and the volume of crystallization is very small. Further investigation is required to confirm cause.

In comparison, the trend in the CM series was more uniform across the sample set. In CaBSi, CM1 and CM2.5 phase C droplets became marginally smaller and more uniformly distributed in size and space throughout regions of phase B (see Appendix for additional images). We also observe that at low concentrations of MoO_3 (~1 mol%) a possible solubility of phase C into phase B occurs. Alternatively, we could be observing a migration of phase C to the outer matrix (phase A). Owing to the heterogeneous nature of the samples, this could also be a result of sampling from the bulk. Qualitatively, there is a migration of Ca from phase C to the other phases and a concurrent shift of Mo from phase A to phases B and C following β-irradiation for samples with MoO_3. For CaBSi without MoO_3, Ca migrates from phase B to phases A and C. Though the trends vary, irradiation induced defects obviously cause reorganization between the phases.

In samples with crystalline $CaMoO_4$, refinement indicates a reduction in cell parameters and a growth in CS for calcium borosilicates (see Table 2). These results imply a relaxation of the unit cell in parallel to a possible diffusion based or precipitated growth of crystallites. The soda-lime borosilicate in this study (CN10) displayed a non-linear CS growth

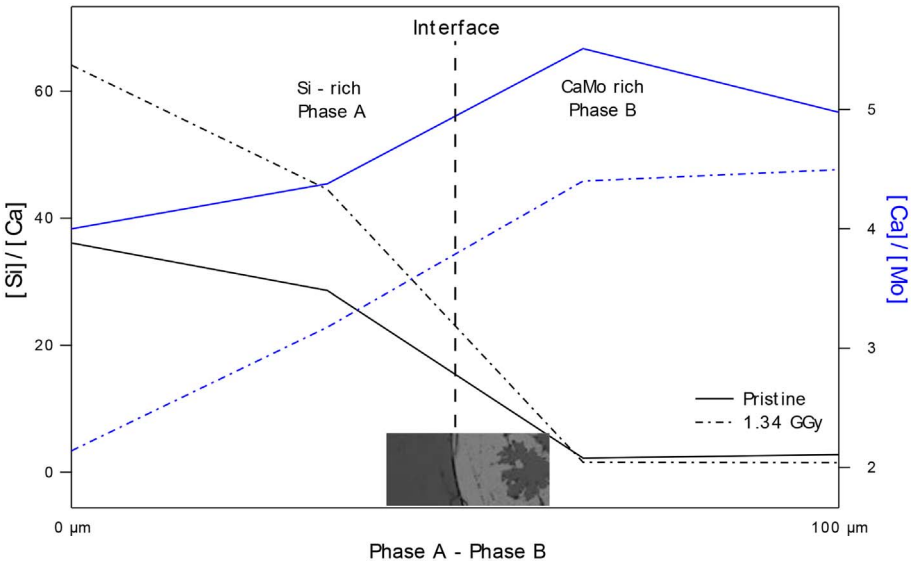

Fig. 9. [Si]/[Ca] and [Ca]\[Mo] ratios from EDS quantitative analysis of CB23 through interface between phase A and B.

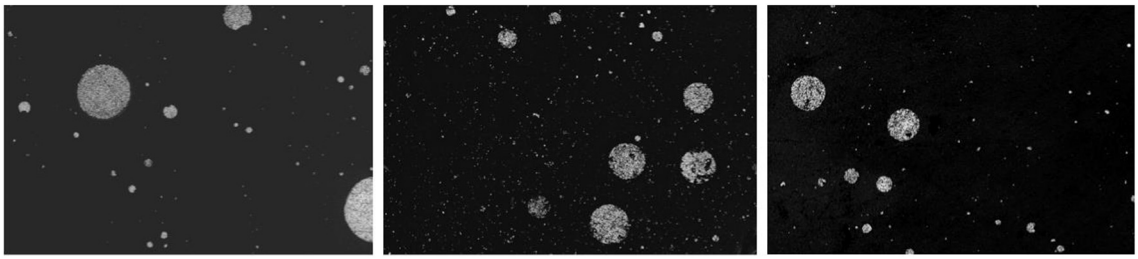

Fig. 10. Scattering of $CaMoO_4$ clusters in CM5 following 0.77 GGy (middle) and 1.34 GGy (left) of β-irradiation.

pattern with dose that was discussed elsewhere [37], but it also had a concurrent relaxation of cell parameters following irradiation. This result indicates that relaxation of the crystal lattice is not directly contingent on the size of clustered particles or the surrounding cationic species and is more dependent on properties of the borosilicate network.

Microstructurally, the crystal clusters observed in CM5 and CM7 also exhibit some changes. In general, the distribution of crystal clusters appears to become smaller and more uniformly distributed (see Fig. 10). The changes in CS following radiation are nominal at 0.77 GGy and reach a maximum change of $\Delta \cong 30 \pm 15$ nm for CM5 and $\Delta \cong 8 \pm 2.2$ nm for CM7 at a dose of 1.34 GGy. Therefore the changes to the size and distribution of crystal clusters following irradiation seem independent of the individual crystallite sizes. Moreover, the overall density of crystals clusters remains fairly constant at the surface, furtherer supporting diffusion-based processes rather than reamorphization. An exception could be very small crystallites, which are difficult to resolve through image analysis.

3.2. Raman analysis

3.2.1. Pristine conditions

Raman spectroscopy can be used to probe short-range order in both amorphous and crystalline phases and therefore provides a useful tool in assessing average changes to bonding order as a function of changing composition. The amorphous phases in both the CB and CM series have several characteristic Raman vibrations associated with silicates and borates as seen in Figs. 11–13. These bands indicate a degree of phase separation into *Si*-rich and B-rich domains following synthesis.

Raman spectra in Figs. 11–13 have standard borosilicate broad bands between ~450–520 cm^{-1} (R-Band) attributed to mixed *Si*—O—Si and Si—O—B bending and rocking [29,38–40], as well as B—O—B rocking (~500 cm^{-1}) [41]. Additional overlapping bands between 850 and 1250 cm^{-1} represent Si—O stretching vibrational modes for Q^n units that represent SiO_4 tetrahedra with *n* bridging oxygen [42] and a weak band around ~800 cm^{-1} is attributed to O—Si—O symmetric bond stretching associated with motions of Si atoms against its oxygen cage [39,43,44]. A narrow band around ~807 cm^{-1} is assigned to the symmetric vibrations of 6-membered boroxyl rings of BO_3-triangles [44–46] and a low intensity broad band around ~1445 cm^{-1} is associated with $B—O^-$ bond elongation in metaborate chains and rings [38]. These groups of Raman vibrations are classically assigned to silicates and borates, respectively [40,43]. In some samples there are additional bands between ~910–930 cm^{-1}. The peak at ~910 cm^{-1} is associated with symmetric stretching vibrational modes of $(MoO_4)^{2-}$ tetrahedral units in amorphous systems [47], while a broader peak ~923 cm^{-1} is assigned to symmetric Si—O stretching of chains with non-bridging oxygens [39,40].

In contrast to the broad bands of the amorphous phase indicating structural disorder, the crystalline phase powellite with C_{4h} point symmetry exhibits several sharp peaks. These peaks are assigned to the lattice vibrations for internal $(MoO_4)^{2-}$ modes in powellite and are as follows: $\nu_1(A_g)$ 878 cm^{-1}, $\nu_3(B_g)$ 848 cm^{-1}, $\nu_3(E_g)$ 795 cm^{-1}, $\nu_4(E_g)$ 405 cm^{-1}, $\nu_4(B_g)$ 393 cm^{-1} and $\nu_2(A_g + B_g)$ 330 cm^{-1} [48]. These modes represent symmetric elongation of the molybdenum tetrahedron, asymmetrical translation of double degenerate modes, symmetric and asymmetrical bending, respectively [49]. All of these vibrational modes can be observed in GCs with crystalline $CaMoO_4$, such as CM7 (Fig. 12), CM5 and CN10, while some can also be seen in phase B of heterogeneous multi-amorphous phase samples.

The concentration effect of MoO_3 can be observed in the Raman spectra of Fig. 11, where a similar pattern for the Si network is observed in all samples in the CM series. The variation in the R band can be attributed to 6-membered (~450 cm^{-1}) versus 4-membered rings

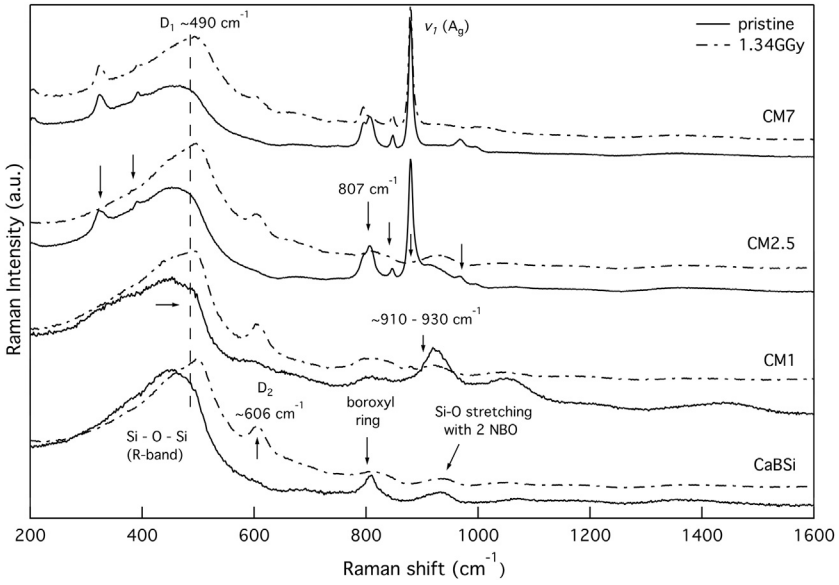

Fig. 11. Raman spectra of *Si*-rich matrix (phase A) in the CM series with increasing fractions of MoO_3 at pristine conditions and following 1.34 GGy. Vertical arrows indicate intensity changes and horizontal lines indicate peak shifts induced by irradiation.

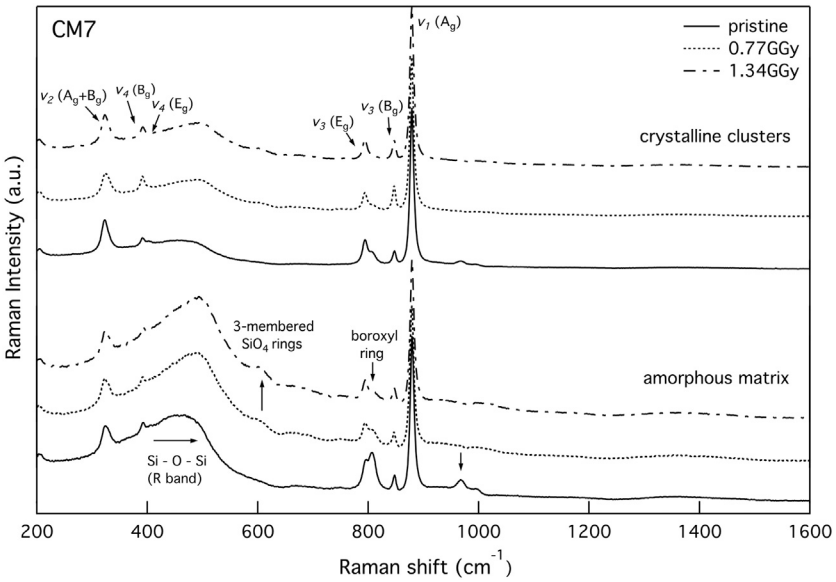

Fig. 12. Raman spectra of amorphous phase A and crystal clusters in CM7 at pristine conditions and following irradiation.

(~490 cm^{-1}), the latter of which has smaller inter-tetrahedral angles and is referred to as the defect D_1. As 1 mol% MoO_3 is introduced into the system, there is growth of the band ~930 cm^{-1} and a shift in the distribution of the R-band favoring higher wavenumbers. This occurs along with a narrowing of the boroxyl ring band and a marginal growth in the low intensity B—O^- bond elongation broad band. These observations indicate a change in the ring structure of Si and B structural units that could be indicative of glass-in-glass phase separation.

As we continue to increase [MoO_3] to 2.5–7.0 mol%, there is growth of $(MoO_4)^{2-}$ vibrational modes and a reduction of the overlapping bands ~910–930 cm^{-1}, indicating further order in the molybdenum environment and eventual crystallization of $CaMoO_4$. This coincides with a broadening of the R band and growth of the sharp boroxyl ring peak. CM2.5 depicts some $(MoO_4)^{2-}$ vibrational modes, though there is no crystalline $CaMoO_4$ according to XRD and SEM imaging. This result suggests either very small crystallites less than 1 vol% in density exist that are beyond detection limits. Or it suggests an amorphous precursor environment to crystallization, which has a similar $(MoO_4)^{2-}$ structure in the amorphous phase.

The Raman spectra for both the amorphous matrix and the crystalline phase of CM7 are illustrated in Fig. 12. An amorphous contribution is evident in both phases, further supporting imaging conclusions that crystals cluster into aggregates rather than forming larger single crystals. We also note that $(MoO_4)^{2-}$ vibrational modes associated with powellite are present in both phases, indicative of nanoparticles dispersed in the amorphous matrix that cannot be observed using SEM. Or similar to that which was predicted from the spectra of CM2.5, it could indicate that $(MoO_4)^{2-}$ groups have a similar structure

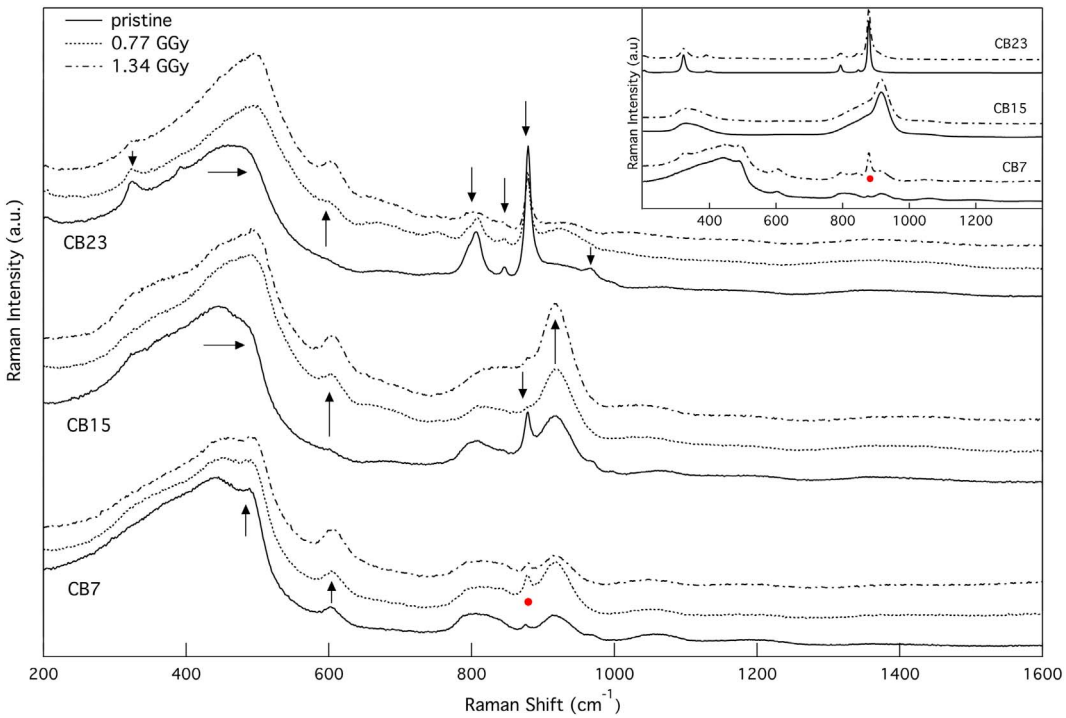

Fig. 13. Raman spectra of the CB series with increasing fractions of B_2O_3 and as a function of increasing dose. Main spectra are of *Si*-rich (phase A) regions, while insert represents CaMo-rich (phase B) regions. Vertical arrows indicate intensity changes and horizontal lines indicate peak shifts following irradiation. Red circle indicates $(MoO_4)^{2-}$ vibration. (For interpretation of the references to colour in this figure legend, the reader is referred to the web version of this article.)

in both the amorphous and crystalline phase.

The CB series similarly has characteristics of a silica-like phase. In these samples there are also two contributions in R band around ~440 cm^{-1} and ~490 cm^{-1} (D_1) that are similar to those in the CM series. However, the spectra for phase A in Fig. 13 also exhibits a weak broad band (~800 cm^{-1}) associated with symmetric vibrations of Si atoms around bridging oxygens and a defect band around ~606 cm^{-1} (D_2) involving partially broken bonds in SiO_4 tetrahedra or the breathing of three-membered SiO_4 rings [50] at low concentrations of B_2O_3. Increasing [B_2O_3] causes a broadening of the R band and D_1, along with growth in the intensity of boroxyl rings (~807 cm^{-1}) that subsequently causes a dampening of the O—*Si*—O stretching vibration (~800 cm^{-1}). This alteration occurs alongside a reduction in the intensity of the D_2 vibrational mode. Therefore the appearance of O—⊜ Si—O stretching and D_2 must be dependent on a high [SiO_2] content. Furthermore, as [B_2O_3] increases the Raman spectra take on more characteristics of borates.

There is also the emergence of $(MoO_4)^{2-}$ vibrational modes as [B_2O_3] increases (see Fig. 13). In CB7 we can see the Raman band at ~878 cm^{-1}, which progressively grows in intensity with [B_2O_3]. In CB23 we can see the emergence of $(MoO_4)^{2-}$ vibrational modes at ~325 cm^{-1}, ~400 cm^{-1}, ~795 cm^{-1} and ~847 cm^{-1} as well. The growth of these modes occurs alongside a dampening in the bands lying between 910 and 930 cm^{-1}. These observations indicate increased order of $(MoO_4)^{2-}$ units towards a more crystalline phase with increasing [B_2O_3]. This is the case, despite no crystallization being detected by XRD in these samples.

In phase B of the CB series (insert of Fig. 13), mostly $(MoO_4)^{2-}$ vibrational modes are observed for [B_2O_3] ≥ 15 mol%. There is also very little contribution from a silica-like phase. This observation supports the theory that phase B is poor in Si and presumably rich in boron.

3.2.2. Radiation effects

Following β-irradiation there are modifications to the Raman spectra of all samples (see Fig. 11). In the CM series there is emergence of the D_2 defect peak and growth of D_1. A shift in the broad Si—O—Si band to higher wavenumbers by ~15–20 cm^{-1} is also observed, which indicates a significant decrease in the Si—O—Si bending angle. This shift is similar to that which is observed for SiO_2 glass under irradiation [51]. Radiation also causes a significant reduction in the intensity of the boroxyl ring vibrational mode. These changes collectively imply a decrease in the ring size of network formers in the amorphous phase A. These modifications occur alongside a reduction in the amplitude and full-width half maximum (fwhm) of $(MoO_4)^{2-}$ vibrational modes in heterogeneous amorphous systems, indicating significant disorder that prevents crystallization.

In GCs, changes to both the crystalline and amorphous phase can be observed. The Raman spectra of crystal clusters in CM7 shows a broadening of the internal $(MoO_4)^{2-}$ modes in powellite (Fig. 12), which is similarly observed in the residual glass phase, along with a dampening of intensity in said modes. This modification is likewise seen for CM5 and CN10. Broadening is associated with greater structural disorder, so radiation is impacting the average crystal quality. In the amorphous phase A of GCs, a shift of the Si—O—Si broadband to higher wavenumbers, as well as emergence of the three-membered SiO_4 ring breathing mode D_2 is observed. These changes occur alongside a reduction in the intensity of Raman modes ~800 cm^{-1} representing O—Si—O vibrations and boroxyl rings. These changes are similar to those occurring in phase A of heterogeneous amorphous samples in the CM series.

In the CB series, a shift of ~3–15 cm^{-1} in the R band to higher wavenumbers and growth of D_1 is similarly observed following irradiation. There is also growth in the intensity of the D_2 defect peak and dampening of the boroxyl ring band, which was also seen in the CM series. Concurrent to these modifications, a growth of the vibrational bands between ~910–930 cm^{-1} is also observed in Fig. 13 together with a reduction in the amplitude and fwhm of $(MoO_4)^{2-}$ vibrational modes for samples with [B_2O_3] ≥ 15 mol%. An exception is observed in CB7 irradiated to 0.77 GGy, which exhibits a growth in intensity of the $(MoO_4)^{2-}$ vibrational mode ~ 878 cm^{-1}. This growth is mirrored by the minor crystal content discovered by EBSD in this sample.

3.3. Irradiation-induced defect structure

Electron Paramagnetic Resonance spectroscopy is a sensitive tool to describe punctual defects induced in glasses by β-irradiation. Prior to irradiation, all of the samples exhibit no electronic defects at room temperature, thus all observations are a result of irradiation. Silicon peroxy radicals (Oxy) (≡Si—O—O·) [52], E′ centers (≡*Si*$^-$) [53], HC_1 centers (≡Si—O·Na^+) [54,55], and boron oxygen hole centers (BOHC) (≡B—O·) [30] have all been previously detected in borosilicates and are also observed in this study with varying compositional effects.

In the CM series the following defect centers were empirically determined by comparison to literature: $E'_{avg.}$ (g ~ 1.9980); BOHC (g ~ 2.0008, 2.0140, 2.0295); Oxy (g ~ 2.0020, 2.0100, 2.0360); and Mo^{6+} reduction to Mo^{5+} (g ~ 1.94) [56,57]. Increasing the inclusion of MoO_3 resulted in a change to the defect distribution and concentration of defects. For starters, a spectral shift with increasing MoO_3 that causes the E′ g-factor to move from ~1.9973 to ~1.9999 is observed (see Fig. 14). There is also a shift in the Mo^{5+} defect towards g ~ 1.93 from g ~ 1.95 as $CaMoO_4$ crystallizes. This occurs in parallel to a general spectral broadening that increases with both increasing [MoO_3] and dose.

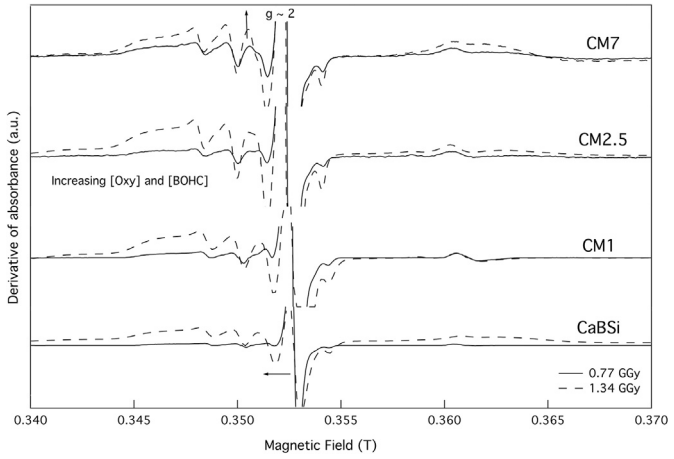

Fig. 14. EPR spectra of the irradiated CM series with increasing [MoO_3] from 0 to 7 mol%.

In the GC CM7 that contains crystalline $CaMoO_4$, we observe significant broadening of the Mo^{5+} band at 1.34 GGy (Fig. 15). This broadening is attributed to Mo^{5+} clustering, where dipole-dipole interactions and exchange of coupled Mo^{5+} ions leads to a superposition of the unresolved hyperfine structure [58,59]. The formation of crystallites is therefore presumed to influence the proximity of defects through enforced rigidity of the crystal network by the surrounding amorphous network.

Furthermore we observe non-linearity in the types of defects formed with increasing [MoO_3]. At 0.77 GGy the [BOHC] relative to [Oxy] increases (see Fig. 14). As dose increases further, we observe a similar trend with an increase in both [Oxy] and [BOHC] defects relative to [E′]. Although E′ is saturated in Figs. 14 and 15, it is evident that BOHC hyperfine spectrum dominates the spectrum with 4 lines per directional component (gx, gy, gz), hence why it is easily observed to increase with dose. In CM2.5 we observe two outliers. The first is that the hyperfine structure of E′ and Oxy defects are more prominent here than in all other spectra in the CM series. The second is that the Mo^{5+} line is narrower, indicating more isolated Mo^{5+} units.

In the CB series we observe a similar set of defects, which are as follows: E′ ($g \sim 2.0002$); BOHC ($g \sim 2.0020$, 2.0150, 2.0284); Oxy ($g \sim 2.0022$, 2.0094, 2.0405); and Mo^{5+} ($g \sim 1.9527$). Variations in the distribution of g tensors are attributed to differences in the bond angles of network formers. There is an additional broad band ~0.6 T wide centered around $g \sim 2.0$ associated with paramagnetic clustering of Gd^{3+} ions. Gd has been previously noted to dampen other defects [56,59], but this is only observed to occur in CBO of this series.

In the CB series the spectral shape remains similar as [B_2O_3] increases from 7 mol% to 23 mol%, with a marginal increase of [BOHC] at higher [B_2O_3] (see Appendix). As dose increases from 0.77 GGy to 1.34 GGy we observe a spectral shift of E′ from $g \sim 2.0002$ to $g \sim 1.9981$ and Mo^{5+} from $g \sim 1.9527$ to $g \sim 1.9495$. We also detect an increase in the [BOHC] EPR spectrum relative to [E′] and [Oxy] spectra, whereas the initial defect structure resembles that of CM1 in Fig. 14. Similar to the CM series, we also observe a broadening of the Mo^{5+} defect with dose, indicative of defect clustering. A compositional effect is also observed in the broadening of this line proportional to increasing [B_2O_3].

In the M series we have $CaMoO_4$ crystallization in all samples, but the distribution of crystallites is dependent on the matrix composition. As a result, we observe a change in the types of defects and therefore EPR spectral shape with composition (see Fig.16). Primarily, an increase of [B_2O_3]/[SiO_2] in the matrix causes a reduction in the relative concentration of all defects. The inclusion of Na at high [MoO_3] causes several changes, including increased reduction of Mo^{5+}, an increase of [BOHC] and a general broadening of all defects.

4. Discussion

4.1. Phase separation

Homogeneity was not achievable in these calcium borosilicate systems without the inclusion of alkali constituents. The formation of phases A, B and C during cooling is hypothesized to occur according to Fig. 17. At the melt temperature it is assumed that the mix is homogenous before separating into immiscible *Si*-rich (phase A) and B/Ca-rich (phase B) domains, the latter of which acts as a carrier for Mo. Within phase B there are still deposits of phase A, which as cooling continues mixes with the surrounding phase B during droplet coalescence to form a new phase C.

The concentration of CaO, B_2O_3 and MoO_3 all influenced the specific microstructure of samples synthesized in this study. The effect of molybdenum is the most easily identifiable as it had both imaging and spectral markers. In literature, molybdenum has a compounding effect on phase separation, not only by inducing precipitation of crystalline molybdates at high concentrations, but also by increasing the immiscibility temperature per mol of MoO_3 and lowering the viscosity and glass-transition temperature (T_g) of the melt [20]. It is also found to affect the glassy matrix by increasing network polymerization through a reduction of NBOs [17,23,60].

In soda-lime borosilicates, Magnin et al. observed a ~ 50 °C increase in the phase separation temperature (T_{PS}) and ~40 °C increase in the crystallization temperature (T_C) of $CaMoO_4$ following an 0.5 mol% increase in MoO_3 [12]. Using this principal we can estimate that the liquid-liquid T_{PS} increases from ~980 °C at 2 mol% MoO_3 to ~1030 °C in CM2.5, assuming that a similar trend is applicable to calcium borosilicate systems. This increase in T_{PS} could account for increased areas of immiscibility and the more spherical shapes these regions are observed to form.

Increases to T_{PS} will result in a greater degree of phase separation and will lower the fictive temperature of the residual matrix [61]. As the synthesis temperature was constant in all systems, microstructural features can be used as a metric to observe changes in the immiscibility temperature in this study. Increasing T_{PS} would allow for the development of multiple phases with varying viscosities that increase or decrease depending on its constituents in proportion to T_{PS}. In this case,

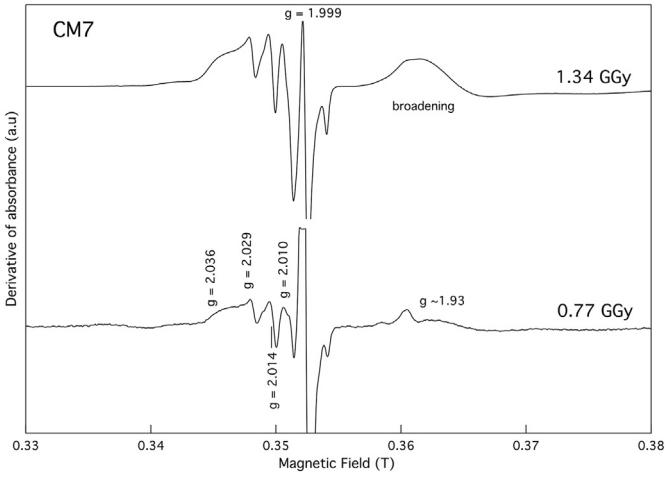

Fig. 15. Detailed EPR spectra of irradiated CM7 (calcium borosilicate with 7 mol% MoO_3).

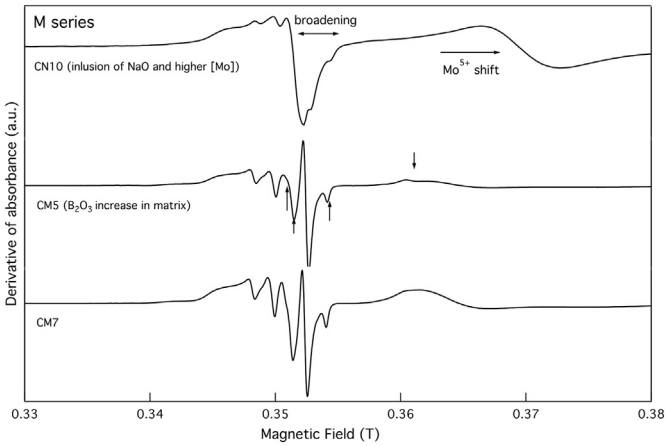

Fig. 16. EPR spectra of GCs in the M series with varying matrices irradiated to 1.34 GGy. From bottom to top: CM7, CM5 (increase of B_2O_3) and CN10 (inclusion of Na and increase of [MoO_3]).

an increase to T_{PS} would cause the lower viscosity separated phase B to coalesce for a longer period of time during cooling forming larger regions. Furthermore, the higher viscosity *Si*-rich phase would cause the cation-rich phase B deposits to combine into the lowest possible surface area, hence why more spherical deposits are observed with increasing [MoO_3]. At lower [MoO_3], elongation of separated phases (see Fig. 1a, b) are attributed to merging of smaller regions of phase B when the viscosity of the two phases is more similar as a result of T_{PS} being closer to T_g. Therefore increasing [MoO_3] enhances the immiscibility properties in the SiO_2-B_2O_3 system and thus promotes secondary phase formation during synthesis. It further enables the amorphous phases to reach a state closer to metastable equilibrium, as the change in temperature between T_{PS} and T_g becomes larger.

These observations indicate that an analogous theory can be proposed for calcium borosilicate systems, in which increasing [MoO_3] also causes an increase in T_{PS} and T_C. As all the samples in this study were heterogeneous, we can further assume that T_{PS} and T_C are higher in calcium borosilicates than they are in soda-lime borosilicates. The higher field strength of Ca^{2+} relative to Na^+ could be promoting the separation of Mo^{6+}, hence the observed heterogeneity. Quintas theorized that increasing the modifier field strength would promote the formation of NBOs in the silica network via changes to the boron coordination [22] and thus encourage phase separation. Correspondingly, we can conclude that in the absence of alkali ions the phase separation tendencies increase with only Ca ions present, as it affects both the separation of Mo^{6+} and glass-in-glass separation.

In calcium borosilicates with [MoO_3] ≥ 5 mol% $CaMoO_4$ crystals are formed. These crystals are observed to form in clusters, which has not been observed to occur in soda-lime borosilicates [37]. The spherical nature of crystallites supports a nucleation and growth mechanism, while the formation of aggregates indicates a high melt viscosity of the surrounding matrix. These observations support the theory that calcium borosilicates have a higher T_{PS} and T_C than soda-lime borosilicates when MoO_3 is introduced into the system.

Molybdates are predicted to form in depolymerized regions of the glass [4,15,25], therefore large depolymerized domains must have been created by liquid-liquid phase separation during synthesis. Prior to crystallization, $(MoO_4)^{2-}$ tetrahedra in these domains are predicted to take a similar form in the Ca-rich phase B to that of crystalline $CaMoO_4$. This notion is based on the Raman spectra of CM2.5 in Fig. 11, which exhibits $(MoO_4)^{2-}$ vibrational modes, though this sample is completely amorphous according to XRD. Molybdenum not crystallized has been previously theorized to be trapped in an amorphous phase of $CaMoO_4$ in soda-lime borosilicates [19], and the same appears true in calcium borosilicates. Therefore the structure and local environment of molybdenum tetrahedra appear independent of the cationic species and are more related to the properties and connectivity of network formers.

The formation of crystallites from similarly structured amorphous precursor environments seemed driven by concentration and mobility of Ca and Mo ions. Quantitative analysis indicates that [Ca] is highest in the center of these clusters and is localized to regions around precipitates in the amorphous phase. Conversely, [Mo] is highest around the internal periphery of crystal clusters. These results allude to a process of phase separation in which the level of borosilicate network reticulation and the formation of NBO channels influences the migration of cations and clustering of insoluble $(MoO_4)^{2-}$ species. It further highlights the immiscibility of $(MoO_4)^{2-}$ units within a *Si*-rich phase. These observations also reflect the quenching technique used for fabrication, in which the amorphous phase exerts rigidity on the distribution of ionic species. A slower cooling may have altered the distribution of Ca species more homogenously and therefore altered the distribution of $CaMoO_4$ crystals.

The sintering process also affected the initial strain within $CaMoO_4$ crystals. While XRD confirmed the presence of a single crystalline

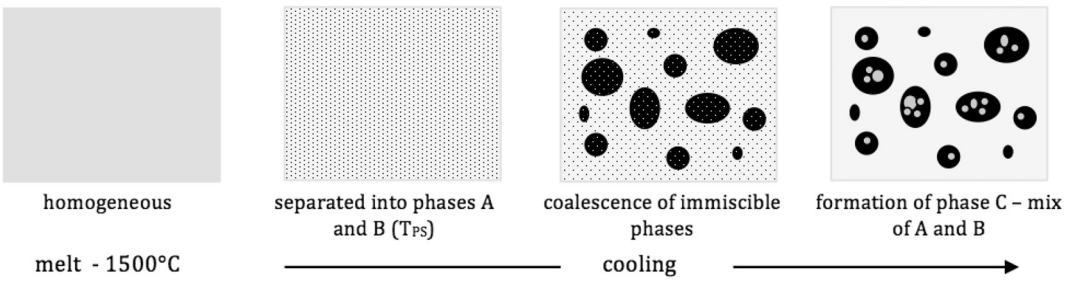

Fig. 17. Schematic of glass-in-glass phase separation hypothesized in calcium borosilicates.

phase, the lattice parameters determined by refinement are initially higher than that of $CaMoO_4$ monocrystals ($a = 5.222$ Å and $c = 11.425$ Å [62]). This observation has been previously recorded for soda-lime borosilicates employing a similar fabrication technique [12,63] and emphasizes how the properties of a glassy phase can increase the lattice energy of embedded crystal phases [64].

The lattice parameters of powellite crystals were not only affected by synthesis conditions, but also by composition. In this study, they are observed to decrease as [MoO_3] increases. This reflects the time at which the temperature (T) falls between $T_g < T < T_C$. As [MoO_3] increases, so to does T_{PS} and T_C. As the maximum sintering temperature was constant in this study, an increase in T_C would allow for a longer period of crystal formation and relaxation before the matrix viscosity hinders any further changes (after T_g).

While MoO_3 has several notable effects on microstructure and crystallization, the amount of B_2O_3 similarly inspired multiple metamorphoses. Increasing [B_2O_3] caused growth of the Raman vibrational mode around ~807 cm^{-1} indicating an increase in the concentration of boroxyl rings. This result could indicate increased phase separation between Si and B structural units. This is further supported by microscopy, which observes an increase in the areas of phases B and C in the embedded microstructure as [B_2O_3] increases. These observations indicate: 1) increased phase separation with increasing [B_2O_3]; 2) that the CaMo-rich phase B is also rich in boron; and 3) that [B_2O_3] affects the melt viscosity. Through Raman spectroscopy we can also see that increasing [B_2O_3] increased the order of $(MoO_4)^{2-}$ units. These observations would suggest that increasing [B_2O_3] also increases the T_{PS}, thus allowing for great order within phase B following synthesis. It also outlines a direct impact of [B_2O_3] on the molybdenum environment.

An oddity is observed in CB7, which exhibits dendritic crystals following 0.77 GGy of irradiation. From glass kinetic studies, $CaMoO_4$ needle shaped crystals are observed between 630 and 810 °C [65] and can be prevented at temperatures around ~1050 °C [18]. Though a similar synthesis technique was used for all samples in the CB series, properties of this specific glass may have enabled slower internal cooling that thus initiated and propagated dendritic growth. Some contaminant from the reagent powders could also have acted as a seed to crystallization, thus lowering the energy barrier of formation. Alternatively, we could be observing radiation-induced crystallization. Given that these crystallites are not observed for CB7 irradiated to 1.34 GGy and are few in quantity and localized to a small area, it is more likely a result of heterogeneities during synthesis. With a low [B_2O_3], the separated phase B is mostly CaMo-rich, which could enable faster growth kinetics and thus the formation of dendrites. Consequently, this observation indicates that though increasing [B_2O_3] increases the order of $(MoO_4)^{2-}$ tetrahedra in the amorphous phase, it also reduces the tendency of crystal formation during cooling by altering the [Ca]\[Mo] ratio in phase B.

The concentration of CaO is also predicted to affect phase separation. Though [CaO] was kept around its limit of 11 mol% [10], glass-in-glass phase separation evidently occurred during synthesis indicating that this limit is lowered in the absence of alkali constituents. This result suggests that the Ca content is an important factor in controlling phase separation and that homogeneity is only possibly when an alkali oxide is also in the composition. It could also imply that the synthesis conditions needed to be altered (physical mixing step at temperature or increased melting temperature) in order to promote a more uniform distribution. Though Ca may have promoted phase separation, it is interesting that calcium borosilicate systems were able to incorporate a higher [MoO_3] around 2.5 mol% than in sodium borosilicates (~1 mol %) before crystallization commenced, albeit in a heterogeneous amorphous network rather than a single amorphous phase. This observation could indicate that while the field strength of Ca^{2+} may promote amorphous phase separation as compared to Na^+, sterics and mobility of larger cations may limit actual crystal formation.

4.2. Radiation effects

Radiation induced transformations can cause amorphization of the crystalline phase, phase separation that could alter the distribution of radionuclides and the formation of defects [26,32,66,67]. These changes can lead to mechanical deficiency or accelerated corrosion tendencies that can significantly alter the chemical durability of the final waste form. While many structural modifications have been observed in homogenous systems, not all of them are negative. Beta irradiation can lead to an increase in polymerization of the borosilicate network [33,68] and can also increase the fracture toughness of the bulk [34] with a dependency on the glass composition.

In this study changes to polymerization were difficult to discern, however an increased network reticulation between B—Si groups is suggested as discussed further below. Several other modification were also observed, some of which were favorable in the prevention of precipitation. Given that samples were primarily heterogeneous, changes to the microstructure were difficult to conclude. In the CM series, there appeared to be an increased integration of immiscible phases B and C. In the CB series this phenomena was dependent on the initial size of phase B and also composition. CB23 appeared to have increased mixing of phase B and C, similar to the CM series, as indicated by a spattering of deposits. Whereas, CB7 and CB15 displayed coalescence of phase C deposits, especially along the A-B interface.

Increased areas of immiscibility were accompanied by growth in the Raman vibrational boroxyl mode ~ 807 cm^{-1}, as describe in the previous section. However, radiation appeared to remediate this in the heterogeneous multi-amorphous phase samples in both the CM and CB series. A shift in the Raman R band to higher wavenumbers was also observed following irradiation in all amorphous phases. This result indicates a reduction in the inter-tetrahedral angles of Si structural units and the growth of the defect band D_1 suggests a more significant contribution from *Si*—O—B bending [40]. Together these results imply a greater connectivity between Si and B structural units following electron irradiation.

Yang et al. hypothesized that Au irradiation caused cleavage of six-membered Si rings that subsequently resulted in the formation of two E′ and NBHOC (non-bringing oxygen hole center) defects. The resulting fragments could then be recombined to form smaller rings, thus resulting in growth of the Raman defect bands D_1 and D_2 [69]. As β-irradiation also causes growth in these Raman modes, we can predict that the same structural modifications are taking place following electronic energy deposition. Furthermore, the reduction in the intensity of the Raman boroxyl mode and the production of BOHCs with dose suggests that an analogous theory can be made for six-membered boron oxide rings (see Fig. 18).

Krogh-Moe and Walrafen et al. observed a similar reduction in intensity of the Raman boroxyl mode for vitreous boron oxide heat treated from 260 to 1000 °C, where thermal events resulted in a structural reorganization of primarily boroxyl groups to a random network of BO_3 triangles [41,46]. Thus β-irradiation is predicted to replicate certain temperature based effects and cause larger ring cleavage and reformation of smaller rings in both B-rich and *Si*-rich regions. This occurrence would constitute a beneficial increase in the integration between network formers. This ring cleavage could be a contributing factor to morphological changes, or specifically an increased mixing between phase B and C, which is observed in some samples.

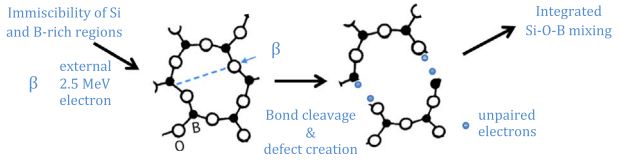

Fig. 18. Hypothesized boroxyl ring cleavage and creation of electronic defects following β-irradiation that causes observed longer-range structural modifications.

In GCs with [MoO_3] exceeding 2.5 mol%, $CaMoO_4$ crystal were formed that were also affected by irradiation. The Scherrer CS appeared to marginally increase with dose, which was concurrent to a reduction in cell parameters in CM7 and CM5. The change in CS induced by irradiation is likely due to diffusion-based growth of very small crystallites or particles (< 1 μm) moving towards a larger cluster. Ca and Mo migration across the crystal cluster-glass interface is implied by EDS analysis. This migration may be due to changes in the charge compensation of different units thus resulting in different [Si]/[Ca] and [Ca]/[Mo] ratios in the various phases following irradiation. If Ca^{2+} migration occurs within these GCs, it is presumed to transpire primarily from the sublattice in which nanocrystallites are embedded, rather than the crystallites themselves. Therefore the crystallites maintain a $CaMoO_4$ composition, despite any ion diffusion.

The reduction in powellite cell parameters is attributed to a relaxation process induced by the added energy from β-impingement. As previously mentioned, the fabrication process causes the cell parameters to be higher than single crystals, which irradiation aids in remediating. $CaMoO_4$ as a single crystal has been previously observed stable against amorphization following Ar-irradiation, which created 5 dpa of structural modifications [48] and low energy electron irradiation produced through in-situ TEM [70]. This study proves that $CaMoO_4$ is also stable with minimal alteration in a calcium borosilicate for up to 1.34 GGy of β-irradiation, though crystals may migrate through the surrounding amorphous network. Despite dampening of crystalline Raman modes and possible migration of Ca and Mo species, all $(MoO_4)^{2-}$ vibrational modes and diffractions peaks are detectable by Raman spectroscopy and XRD before and after irradiation, indicating rigidity of the $CaMoO_4$ structure and composition.

The defects observed in this study follow those observed in literature with a variance corresponding to changes in composition. A change in the glass composition can alter alkaline processes and therefore [BOHC] defect relative to [Oxy]. Both MoO_3 and B_2O_3 influenced the defect distribution, the former of which having a greater impact in terms of Mo^{6+} reduction and defect broadening. Whereas B_2O_3 inclusion appeared correlated to the defect structure of the borosilicate network, and primarily the growth of the BOHC hyperfine structure. In heterogeneous multi-amorphous systems, the separation of B-rich regions during synthesis could either lead to a dominant site for defect creation or it could indicate that while other defects are absorbed in structural modifications, these trace BOHC defects remain.

Following irradiation a general broadening in the defect structure was observed, indicating a change in the dipolar interactions of paramagnetic species in the vicinity of other defects. This could imply Mo^{5+} clustering, which could be linked to the concentration effects on heterodistribution. However, it is difficult to determine which defect interactions are causing specific broadening, as the spectra are very complex. Therefore we can only make observations on the bulk response, even if the intrinsic defects are localized. These defects could enable channel formation that would ease migration of crystalline $CaMoO_4$ species. Alternatively, defects absorbed in longer order structural modification could be increasing *Si*—B mixing, as is indicated by Raman spectroscopy.

4.3. Mo solubility

Crystallized molybdates and diluted molybdenum anions within a glassy framework are predicted to have a similar structure, hence why molybdenum has a limited solubility in glasses [24]. In this sample set we observed a preference for $(MoO_4)^{2-}$ units to be located in a Ca-rich phase B, which is also predicted to be rich in boron. Hence why increasing [B_2O_3] reduced the potential solubility limit and increased the order of $(MoO_4)^{2-}$ anions to a more crystalline structure, as there was increased competition for limited Ca^{2+} charge compensators.

As radiation commenced, changes to the molybdenum order are indicated by the relative shift in [Mo] between phases and the dampening of Raman $(MoO_4)^{2-}$ vibrational modes. These changes can be correlated to the reduction of Mo^{6+}, as alterations to the oxidation state of molybdenum are known to accompany phase separation. Yellow phase precipitation in particular is prevalent for Mo(IV) and changes to the redox conditions during preparation are known to influence the solubility limit [21]. As previously mentioned, glasses synthesized under reducing conditions have an increased solubility of MoO_3 [5]. This is an important factor to consider, as there is a proportional reduction of Mo^{6+} to Mo^{5+} induced by β-irradiation and compounded with increasing dose (Figs. 14 and 15). Indeed, a significant decrease in the order of $(MoO_4)^{2-}$ tetrahedra in the amorphous phase of the CB series was observed as dose increases. Raman spectra in Fig. 13 illustrate a significant dampening of $(MoO_4)^{2-}$ vibrational bands in the *Si*-rich phase A and significant broadening in the CaMo-rich phase B. This occurs alongside an increase in Mo^{6+} reduction, according to EPR. These results would allude to an increased Mo solubility, or at least an increased degree of disorder that prevents crystallization with dose when the concentration of MoO_3 is around ~2.5 mol%, which is the case for all samples in the CB series.

A similar effect was also observed in the Raman spectra of the CM series. In these systems, β-irradiation is favorably creating structural disorder, thereby averting $CaMoO_4$ crystallization in heterogeneous multiamorphous phase samples (CM1, CM2.5). In GCs with [MoO_3] > 2.5 mol% a dampening of crystalline Raman vibrational modes was also observed, as well as migration of Ca and Mo ions between amorphous phase A and crystalline phase B. It is unlikely that beta irradiation is causing amorphization of $CaMoO_4$, rather that there is increased disorder in the sublattice surround the crystalline phase as all the Raman modes are visible post irradiation. This is not the case in heterogeneous multiamorphous phase samples ([MoO_3] ≤ 2.5 mol%), where significant dampening of $(MoO_4)^{2-}$ Raman modes indicates multi-amorphous phase integration and amorphization of any nanocrystallites that are not detected by SEM or XRD. Increasing [MoO_3] also resulted in an increased Mo^{6+} reduction, which was similarly observed in soda-lime borosilicates [56]. Therefore, the solubility of molybdenum is assumed to increase with accumulated decay if there is no prior crystallization.

The EPR spectral shift of the Mo^{5+} defect towards g ~ 1.93 from g ~ 1.95 as $CaMoO_4$ crystallizes is indicative of a transformation from a bonded ion to a free ion [5]. Though EPR detects trace defects, this change can reflect those absorbed by structural transformations. This observation indicates that while the $CaMoO_4$ crystal structure appeared unchanged according to XRD, this may change with increasing dose.

5. Conclusions

In order to increase the incorporation of low solubility molybdenum groups in nuclear waste materials, new compositions are being investigated. This study addressed the behavior of calcium borosilicates as a function of B_2O_3 and MoO_3 concentrations when subjected to β-irradiation in order to determine factors affecting phase separation and crystallization. The synthesized glasses and GCs were multiphase with a unique embedded immiscibility microstructure or clustered crystallization, respectively. For a normalized calcium borosilicate system, increasing MoO_3 resulted and in an increase of T_{PS} and progressive order in the $(MoO_4)^{2-}$ region until crystallization commences for [MoO_3] > 2.5 mol%. An increase in the T_{PS} is predicted to account for the more spherical morphology observed with increasing [MoO_3] as the change in viscosity between phases becomes larger. Increasing [B_2O_3] similarly caused greater areas of immiscibility as it acted as a carrier phase for molybdenum and increased the order of $(MoO_4)^{2-}$ tetrahedra in the amorphous phase. β-irradiation on the order of 100 + years of storage induced favorable qualities by increasing structural disorder of the CaMo-rich regions in multi-amorphous phase samples in proportion to an increase in Mo^{6+} reduction, thereby preventing the crystallization of $CaMoO_4$ entities. It also reduced the tendency of glass-in-

glass phase separation through the formation of intrinsic defects that caused alterations in the borosilicate ring structures and thus affected the distribution of network formers. Integrated *Si*-O-B mixing is observed by the reduction of the Raman boroxyl ring vibrational mode and growth of defects D_1 and D_2 following irradiation, which indicates electron cleavage of 6-membered rings and formation of smaller rings. Radiation was further found not to induce or propagate crystallization, but it did enable reorganization of crystallites and Ca cations in GCs. The tendency of $CaMoO_4$ crystals to form and aggregate is therefore most likely dependent on the propensity for phase separation during synthesis and the initial composition, rather than irradiation-induced. In heterogamous amorphous samples radiation beneficially created disorder, thus reducing the probability of precipitation, despite varying influences by B_2O_3 and MoO_3.

Abbreviations

GC	glass ceramic material
Gy	unit of absorbed dose
R7T7	French nuclear waste glass composition
SON68	inactive version of R7T7
NBO	non-bridging oxygen
Oxy	silicon peroxy radicals
BOHC	boron oxygen hole center
T_g	glass-transition temperature
T_{PS}	phase separation temperature
T_C	crystallization temperature

Funding sources

University of Cambridge, Department of Earth Sciences and EPSRC (Grant No. EP/K007882/1) for an IDS. Cambridge Philosophical Society for a supplementary research grant.

Acknowledgements

The authors would like to thank EPSRC for financial support of this doctorate project and the EMIR network for irradiation time. We would also like to acknowledge Dr. Giulio Lampronti at the University of Cambridge for his help in performing EBSD and expertise in the area of crystallography. Mention should also be made to Olivier Cavani at LSI who monitored the irradiation experiment on the SIRIUS beamline. Several members in the Department of Earth Sciences (Robin Clarke, Chris Parish, Dr. Iris Buisman) and those from the Department of Material Science and Metallurgy (Lata Sahonta, Rachel Olivier) aided in access to facilities and sample preparation, as well as training on analytical equipment.

Appendix A. Supplementary information/appendices

SI_Appendix.pdf – details of Rietveld refinement, additional SEM images, examples of EDS quantitative analysis and ratio determination, EBSD results and additional EPR spectra. Supplementary data associated with this article can be found in the online version, at http://dx.doi.org/10.1016/j.jnoncrysol.2017.06.018.

References

[1] W.E. Lee, M.I. Ojovan, M.C. Stennett, N.C. Hyatt, Immobilisation of radioactive waste in glasses, glass composite materials and ceramics, Adv. Appl. Ceram. 105 (2006) 3–12, http://dx.doi.org/10.1179/174367606X81669.
[2] S. Peuget, J.M. Delaye, C. Jégou, Specific outcomes of the research on the radiation stability of the French nuclear glass towards alpha decay accumulation, J. Nucl. Mater. 444 (2014) 76–91, http://dx.doi.org/10.1016/j.jnucmat.2013.09.039.
[3] P. Frugier, C. Martin, I. Ribet, T. Advocat, S. Gin, The effect of composition on the leaching of three nuclear waste glasses: R7T7, AVM and VRZ, J. Nucl. Mater. 346 (2005) 194–207, http://dx.doi.org/10.1016/j.jnucmat.2005.06.023.
[4] G. Calas, M. Le Grand, L. Galoisy, D. Ghaleb, Structural role of molybdenum in nuclear glasses: an EXAFS study, J. Nucl. Mater. 322 (2003) 15–20, http://dx.doi.org/10.1016/S0022-3115(03)00277-0.
[5] A. Horneber, B. Camara, W. Lutze, Investigation on the oxidation state and the behaviour of molybdenum in silicate glass, MRS Proc. Sci. Basis Nucl. Waste Manag. V, Vol. 11 Berlin, 1981, pp. 279–288.
[6] E. Nicoleau, S. Schuller, F. Angeli, T. Charpentier, P. Jollivet, A. Le Gac, M. Fournier, A. Mesbah, F. Vasconcelos, Phase separation and crystallization effects on the structure and durability of molybdenum borosilicate glass, J. Non-Cryst. Solids 427 (2015) 120–133, http://dx.doi.org/10.1016/j.jnoncrysol.2015.07.001.
[7] M.I. Ojovan, W.E. Lee, An Introduction to Nuclear Waste Immobilisation, Elsevier, 2005.
[8] J.V. Crum, B.J. Riley, L.R. Turo, M. Tang, A. Kossoy, Summary Report: Glass-Ceramic Waste Forms for Combined Fission Products, Richland, 2011.
[9] J.M. Gras, R. Do Quang, H. Masson, T. Lieven, C. Ferry, C. Poinssot, M. Debes, J.M. Delbecq, Perspectives on the closed fuel cycle - implications for high-level waste matrices, J. Nucl. Mater. 362 (2007) 383–394, http://dx.doi.org/10.1016/j.jnucmat.2007.01.210.
[10] M. Magnin, S. Schuller, C. Mercier, J. Trébosc, D. Caurant, O. Majérus, F. Angéli, T. Charpentier, Modification of molybdenum structural environment in borosilicate glasses with increasing content of boron and calcium oxide by 95Mo MAS NMR, J. Am. Ceram. Soc. 94 (2011) 4274–4282, http://dx.doi.org/10.1111/j.1551-2916.2011.04919.x.
[11] S. Schuller, O. Pinet, A. Grandjean, T. Blisson, Phase separation and crystallization of borosilicate glass enriched in MoO3, P2O5, ZrO2, CaO, J. Non-Cryst. Solids 354 (2008) 296–300, http://dx.doi.org/10.1016/j.jnoncrysol.2007.07.041.
[12] M. Magnin, Étude des processus de demixtion et de cristallisation au sein de liquides fondus borosilicatÉs riches en oxyde de molybdène, Université Pierre et Marie Curie, 2009.
[13] R. Short, Phase separation and crystallisation in UK HLW vitrified products, Procedia Mater. Sci. 7 (2014) 93–100, http://dx.doi.org/10.1016/j.mspro.2014.10.013.
[14] B.F. Dunnett, N.R. Gribble, R. Short, E. Turner, C.J. Steele, A.D. Riley, Vitrification of high molybdenum waste, Glass Technol. Eur. J. Glass Sci. Technol. Part A 53 (2012) 166–171.
[15] R.J. Short, R.J. Hand, N.C. Hyatt, G. Möbus, Environment and oxidation state of molybdenum in simulated high level nuclear waste glass compositions, J. Nucl. Mater. 340 (2005) 179–186, http://dx.doi.org/10.1016/j.jnucmat.2004.11.008.
[16] N. Chouard, D. Caurant, O. Majérus, J.L. Dussossoy, A. Ledieu, S. Peuget, R. Baddour-Hadjean, J.P. Pereira-Ramos, Effect of neodymium oxide on the solubility of MoO3 in an aluminoborosilicate glass, J. Non-Cryst. Solids 357 (2011) 2752–2762, http://dx.doi.org/10.1016/j.jnoncrysol.2011.02.015.
[17] D. Caurant, O. Majérus, E. Fadel, A. Quintas, C. Gervais, T. Charpentier, D. Neuville, Structural investigations of borosilicate glasses containing MoO3 by MAS NMR and Raman spectroscopies, J. Nucl. Mater. 396 (2010) 94–101, http://dx.doi.org/10.1016/j.jnucmat.2009.10.059.
[18] T. Taurines, B. Boizot, Microstructure of powellite-rich glass-ceramics: a model system for high level waste immobilization, J. Am. Ceram. Soc. 95 (2012) 1105–1111, http://dx.doi.org/10.1111/j.1551-2916.2011.05015.x.
[19] N. Henry, P. Deniard, S. Jobic, R. Brec, C. Fillet, F. Bart, A. Grandjean, O. Pinet, Heat treatments versus microstructure in a molybdenum-rich borosilicate, J. Non-Cryst. Solids 333 (2004) 199–205, http://dx.doi.org/10.1016/j.jnoncrysol.2003.09.055.
[20] Y. Kawamoto, K. Clemens, M. Tomozawa, Effects of MoO3 on phase separation of Na20-B203-Si02 glasses, J. Am. Ceram. Soc. 64 (1981) 292–296.
[21] K. Ishiguro, N. Kawanishi, H. Nagaki, A. Naito, Chemical states of molybdenum in radioactive waste glass, Japan, 1982 (doi: PNCT-N-831-82-01).
[22] A. Quintas, D. Caurant, O. Majérus, T. Charpentier, J.L. Dussossoy, Effect of compositional variations on charge compensation of AlO4 and BO4 entities and on crystallization tendency of a rare-earth-rich aluminoborosilicate glass, Mater. Res. Bull. 44 (2009) 1895–1898, http://dx.doi.org/10.1016/j.materresbull.2009.05.009.
[23] F. Angeli, O. Villain, S. Schuller, S. Ispas, T. Charpentier, Insight into sodium silicate glass structural organization by multinuclear NMR combined with first-principles calculations, Geochim. Cosmochim. Acta 75 (2011) 2453–2469, http://dx.doi.org/10.1016/j.gca.2011.02.003.
[24] D. Caurant, O. Majérus, E. Fadel, M. Lenoir, C. Gervais, O. Pinet, Effect of molybdenum on the structure and on the crystallization of SiO2-Na2O-CaO-B2O3 glasses, J. Am. Ceram. Soc. 90 (2007) 774–783, http://dx.doi.org/10.1111/j.1551-2916.2006.01467.x.
[25] G.N. Greaves, K.L. Ngai, Reconciling ionic-transport properties with atomic structure in oxide glasses, Phys. Rev. B 52 (1995) 6358–6380, http://dx.doi.org/10.1103/PhysRevB.52.6358.
[26] W.J. Weber, R.C. Ewing, C.A. Angell, G.W. Arnold, J.M. Delaye, L.W. Hobbs, D.L. Price, Radiation effects in glasses used for immobilization of high-level waste and plutonium disposition, J. Mater. Res. 12 (1997) 1946–1978.
[27] D.L. Griscom, Trapped-electron centers in pure and doped glassy silica: a review and synthesis, J. Non-Cryst. Solids 357 (2011) 1945–1962, http://dx.doi.org/10.1016/j.jnoncrysol.2010.11.011.
[28] B. Boizot, G. Petite, D. Ghaleb, G. Calas, Radiation induced paramagnetic centres in nuclear glasses by EPR spectroscopy, Nucl. Instrum. Methods Phys. Res., Sect. B Beam Interact. with Mater. Atoms. 141 (1998) 580–584, http://dx.doi.org/10.1016/S0168-583X(98)00102-5.
[29] D.R. Neuville, L. Cormier, B. Boizot, A.M. Flank, Structure of β-irradiated glasses studied by X-ray absorption and Raman spectroscopies, J. Non-Cryst. Solids 323 (2003) 207–213, http://dx.doi.org/10.1016/S0022-3093(03)00308-9.
[30] D.L. Griscom, et al., J. Non-Cryst. Solids 13 (1974) 251–285, http://dx.doi.org/10.

1016/0022-3093(74)90095-7.
[31] N. Ollier, B. Boizot, B. Reynard, D. Ghaleb, G. Petite, β irradiation in borosilicate glasses: the role of the mixed alkali effect, Nucl. Instrum. Methods Phys. Res., Sect. B Beam Interact. with Mater. Atoms. 218 (2004) 176–182, http://dx.doi.org/10.1016/j.nimb.2003.12.014.
[32] K. Sun, L.M. Wang, R.C. Ewing, W.J. Weber, Electron irradiation induced phase separation in a sodium borosilicate glass, Nucl. Instrum. Methods Phys. Res., Sect. B Beam Interact. with Mater. Atoms. 218 (2004) 368–374, http://dx.doi.org/10.1016/j.nimb.2003.12.022.
[33] K.J. Yang, T.S. Wang, G.F. Zhang, H.B. Peng, L. Chen, L.M. Zhang, C.X. Li, F. Tian, W. Yuan, Study of irradiation damage in borosilicate glass induced by he ions and electrons, Nucl. Instrum. Methods Phys. Res., Sect. B Beam Interact. with Mater. Atoms. 307 (2013) 541–544, http://dx.doi.org/10.1016/j.nimb.2012.12.113.
[34] O. Gedeon, J. Lukeš, K. Jurek, Reduced young modulus and hardness of electron irradiated binary potassium-silicate glass, Nucl. Instrum. Methods Phys. Res., Sect. B Beam Interact. with Mater. Atoms. 275 (2012) 7–10, http://dx.doi.org/10.1016/j.nimb.2011.12.017.
[35] G. Eriksson, P. Wu, M. Blander, A.D. Pelton, Critical evaluation and optimization of the thermodynamic properties and phase diagrams of the MnO-SiO2 and CaO-SiO2 systems, Can. Metall. Q. 1 (1994) 13–21, http://dx.doi.org/10.1007/bf02663141.
[36] R.W. Cheary, A.A. Coelho, J.P. Cline, Fundamental parameters line profile fitting in laboratory diffractometers, J. Res. Natl. Inst. Stand. Technol. 109 (2004) 1–25, http://dx.doi.org/10.6028/jres.109.002.
[37] K.B. Patel, B. Boizot, S.P. Facq, G.I. Lampronti, S. Peuget, S. Schuller, I. Farnan, β-Irradiation effects on the formation and stability of $CaMoO_4$ in a soda lime borosilicate glass ceramic for nuclear waste storage, Inorg. Chem. (2017) acs.inorgchem.6b02657, , http://dx.doi.org/10.1021/acs.inorgchem.6b02657.
[38] J. de Bonfils, S. Peuget, G. Panczer, D. de Ligny, S. Henry, P.-Y. Noël, A. Chenet, B. Champagnon, Effect of chemical composition on borosilicate glass behavior under irradiation, J. Non-Cryst. Solids 356 (2010) 388–393, http://dx.doi.org/10.1016/j.jnoncrysol.2009.11.030.
[39] M.H. Mangham, A. Hushur, T. Sekine, J. Wu, J.F. Stebbins, Q. Williams, Raman, Brillouin, and nuclear magnetic resonance spectroscopic studies on shocked borosilicate glass, J. Appl. Phys. 109 (2011), http://dx.doi.org/10.1063/1.3592346.
[40] T. Furukawa, W.B. White, Raman spectroscopic investigation of sodium borosilicate glass structure, J. Mater. Sci. 16 (1981) 2689–2700, http://dx.doi.org/10.1007/BF00552951.
[41] G.E. Walrafen, S.R. Samanta, P.N. Krishnan, Raman investigation of vitreous and molten boric oxide, J. Chem. Phys. 72 (1980) 113–120, http://dx.doi.org/10.1063/1.438894.
[42] D. Manara, A. Grandjean, D.R. Neuville, Structure of borosilicate glasses and melts: a revision of the Yun, Bray and Dell model, J. Non-Cryst. Solids 355 (2009) 2528–2531, http://dx.doi.org/10.1016/j.jnoncrysol.2009.08.033.
[43] D. Manara, A. Grandjean, D.R. Neuville, Advances in understanding the structure of borosilicate glasses: a Raman spectroscopy study, Am. Mineral. 94 (2009) 777–784, http://dx.doi.org/10.2138/am.2009.3027.
[44] W.L. Konijnendijk, J.M. Stevels, The structure of borate glasses studied by Raman scattering, J. Non-Cryst. Solids 18 (1975) 307–331, http://dx.doi.org/10.1016/0022-3093(75)90137-4.
[45] J. Goubeau, H. Kellaer, RAMAN-Spektren und Struktur von Boroxol-Verbindungen (German), ZAAC - J. Inorg. Gen. Chem. 272 (1953) 303–312, http://dx.doi.org/10.1002/zaac.19532720510.
[46] J. Krogh-Moe, The structure of vitreous and liquid boron oxide, J. Non-Cryst. Solids 1 (1969) 269–284, http://dx.doi.org/10.1016/0022-3093(69)90025-8.
[47] N. Chouard, D. Caurant, O. Majérus, J.L. Dussossoy, S. Klimin, D. Pytalev, R. Baddour-Hadjean, J.P. Pereira-Ramos, Effect of MoO3, Nd2O3, and RuO2 on the crystallization of soda–lime aluminoborosilicate glasses, J. Mater. Sci. 50 (2015) 219–241, http://dx.doi.org/10.1007/s10853-014-8581-9.
[48] X. Wang, G. Panczer, D. de Ligny, V. Motto-Ros, J. Yu, J.L. Dussossoy, S. Peuget, I. Jóźwik-Biala, N. Bérerd, J. Jagielski, Irradiated rare-earth-doped powellite single crystal probed by confocal Raman mapping and transmission electron microscopy, J. Raman Spectrosc. 45 (2014) 383–391, http://dx.doi.org/10.1002/jrs.4472.
[49] R.L. Frost, J. Bouzaid, I.S. Butler, Raman spectroscopic study of the molybdate mineral szenicsite and com- pared with other paragenetically related molybdate minerals, Spectrosc. Lett. 40 (2007) 603–614.
[50] B. Hehlen, D.R. Neuville, Raman response of network modifier cations in aluminosilicate glasses, J. Phys. Chem. B 119 (2015) 4093–4098, http://dx.doi.org/10.1021/jp5116299.
[51] R.A.B. Devine, Macroscopic and microscopic effects of radiation in amorphous SiO2, Nucl. Instrum. Methods Phys. Res., Sect. B Beam Interact. with Mater. Atoms. 91 (1994) 378–390, http://dx.doi.org/10.1016/0168-583X(94)96253-7.
[52] D.A. Dot, P.L. Higby, D.L. Griscom, An electron spin resonance study of X-irradiated calcium aluminosilicate glasses, J. Non-Cryst. Solids 130 (1991) 41–51, http://dx.doi.org/10.1016/0022-3093(91)90154-X.
[53] R.A. Weeks, The many varieties of E′ centers: a review, J. Non-Cryst. Solids 179 (1994) 1–9, http://dx.doi.org/10.1016/0022-3093(94)90680-7.
[54] D.L. Griscom, Defect structure of glasses, J. Non-Cryst. Solids 73 (1985) 51–77, http://dx.doi.org/10.1016/0022-3093(85)90337-0.
[55] G. Kordas, B. Camara, H.J. Oel, Electron spin resonance studies of radiation damage in silicate glasses, J. Non-Cryst. Solids 50 (1982) 79–95, http://dx.doi.org/10.1016/0022-3093(82)90202-2.
[56] T. Taurines, D. Neff, B. Boizot, Powellite-rich glass-ceramics: a spectroscopic study by EPR and Raman spectroscopy, J. Am. Ceram. Soc. 96 (2013) 3001–3007, http://dx.doi.org/10.1111/jace.12401.
[57] E.W.A. Serwicka, ESR evidence for structural rearrangements occuring upon MoO3 reduction, J. Solid State Chem. 51 (1984) 300–306.
[58] D. Toloman, R. Ciceo-Lucacel, D.A. Magdas, A. Regos, A.R. Biris, C. Leostean, I. Ardelean, The modifier/former role of MoO3 in some calcium-phosphate glasses, J. Alloys Compd. 556 (2013) 67–70, http://dx.doi.org/10.1016/j.jallcom.2012.12.112.
[59] E. Malchukova, B. Boizot, D. Ghaleb, G. Petite, β-Irradiation effects in Gd-doped borosilicate glasses studied by EPR and Raman spectroscopies, J. Non-Cryst. Solids 352 (2006) 297–303, http://dx.doi.org/10.1016/j.jnoncrysol.2005.11.003.
[60] C. Martineau, V.K. Michaelis, S. Schuller, S. Kroeker, Liquid-liquid phase separation in model nuclear waste glasses: a solid-state double-resonance NMR study, Chem. Mater. 22 (2010) 4896–4903, http://dx.doi.org/10.1021/cm1006058.
[61] H. Kobayashi, H. Takahashi, Roles of intermediate-range orders on the glass transition process: fictive temperature, residual entropy, relaxation time and boson peak, J. Non-Cryst. Solids 427 (2015) 34–40, http://dx.doi.org/10.1016/j.jnoncrysol.2015.06.029.
[62] R.M. Hazen, L.W. Finger, J.W.E. Mariathasan, High-pressure crystal chemistry of scheelite-type tungstates and molybdates, J. Phys. Chem. Solids 46 (1985) 253–263, http://dx.doi.org/10.1016/0022-3697(85)90039-3.
[63] C. Mendoza, Caracterisation et comportement sous irradiation de phases powellites dopees terres rares – application au comportement a long terme des matrices de confinement des dechets nuclement Mendoza To cite this version, Universite Claude Bernard, Lyon I, 2010.
[64] R. Webster, M. Lark, Field Sampling for Environmental Science and Management, Routledge, Oxon, UK, 2013.
[65] X. Orlhac, C. Fillet, J. Phalippou, Study of crystallization mechanisms in the French nuclear waste glass, Mater. Res. Soc. Symp. Proc. (1999) 263–270.
[66] G. Gutierrez, S. Peuget, J.A. Hinks, G. Greaves, S.E. Donnelly, E. Oliviero, C. Jégou, Helium bubble formation in nuclear glass by in-situ TEM ion implantation, J. Nucl. Mater. 452 (2014) 565–568, http://dx.doi.org/10.1016/j.jnucmat.2014.06.010.
[67] J.-M. Delaye, S. Peuget, G. Bureau, G. Calas, Molecular dynamics simulation of radiation damage in glasses, J. Non-Cryst. Solids 357 (2011) 2763–2768, http://dx.doi.org/10.1016/j.jnoncrysol.2011.02.026.
[68] B. Boizot, G. Petite, D. Ghaleb, G. Calas, Dose, Dose Rate and Irradiation Temperature Effects in β-irradiated Simplified Nuclear Waste Glasses by EPR Spectroscopy, 283 (2001), pp. 179–185.
[69] T. Yang, Y. Gao, X. Huang, Y. Zhang, M. Toulemonde, J. Xue, S. Yan, Y. Wang, The transformation balance between two types of structural defects in silica glass in ion-irradiation processes, J. Non-Cryst. Solids 357 (2011) 3245–3250, http://dx.doi.org/10.1016/j.jnoncrysol.2011.05.017.
[70] K. Brinkman, K. Fox, J. Marra, J. Reppert, J. Crum, M. Tang, Single phase melt processed powellite (Ba,Ca)MoO_4 for the immobilization of Mo-rich nuclear waste, J. Alloys Compd. 551 (2013) 136–142, http://dx.doi.org/10.1016/j.jallcom.2012.09.049.